SANDIA REPORT

SAND2004-0911
Unlimited Release
Printed March 2004

Focused ion beam techniques for fabricating geometrically-complex components and devices

David P. Adams, Michael J. Vasile, Thomas M. Mayer, and V. Carter Hodges

Prepared by
Sandia National Laboratories
Albuquerque, New Mexico 87185 and Livermore, California 94550

Sandia is a multiprogram laboratory operated by Sandia Corporation,
a Lockheed Martin Company, for the United States Department of Energy's
National Nuclear Security Administration under Contract DE-AC04-94AL85000.

Issued by Sandia National Laboratories, operated for the United States Department of Energy by Sandia Corporation.

Available to DOE and DOE contractors from
U.S. Department of Energy
Office of Scientific and Technical Information
P.O. Box 62
Oak Ridge, TN 37831

Telephone: (865)576-8401
Facsimile: (865)576-5728
E-Mail: reports@adonis.osti.gov
Online ordering: http://www.doe.gov/bridge

Available to the public from
U.S. Department of Commerce
National Technical Information Service
5285 Port Royal Rd
Springfield, VA 22161

Telephone: (800)553-6847
Facsimile: (703)605-6900
E-Mail: orders@ntis.fedworld.gov
Online order: http://www.ntis.gov/help/ordermethods.asp?loc=7-4-0#online

SAND2004-0911
Unlimited Release
Printed March 2004

Focused ion beam techniques for fabricating geometrically-complex components and devices

David P. Adams, Michael J. Vasile, Thomas M. Mayer, and V. Carter Hodges
Thin Film, Vacuum and Packaging Department

Sandia National Laboratories
P.O. Box 5800
Albuquerque, NM, 87185-0959

Abstract

We have researched several new focused ion beam (FIB) micro-fabrication techniques that offer control of feature shape and the ability to accurately define features onto nonplanar substrates. These FIB-based processes are considered useful for prototyping, reverse engineering, and small-lot manufacturing.

Ion beam-based techniques have been developed for defining features in miniature, nonplanar substrates. We demonstrate helices in cylindrical substrates having diameters from 100 μm to 3 mm. Ion beam lathe processes sputter-define 10-μm wide features in cylindrical substrates and tubes. For larger substrates, we combine focused ion beam milling with ultra-precision lathe turning techniques to accurately define 25-100 μm features over many meters of path length. In several cases, we combine the feature defining capability of focused ion beam bombardment with additive techniques such as evaporation, sputter deposition and electroplating in order to build geometrically-complex, functionally-simple devices. Damascene methods that fabricate bound, metal microcoils have been developed for cylindrical substrates.

Effects of focused ion milling on surface morphology are also highlighted in a study of ion-milled diamond.

TABLE OF CONTENTS

Chapter 1: Focused ion beam experimental apparatus

1.1 Description of system

A custom-built focused ion beam system is used for ion milling experiments and process development. The target chamber has a base pressure of $9x10^{-8}$ Torr and contains a precision x-y stage, a sample cassette, a gas doser, a secondary electron detector and a residual gas analyzer. The ion column is located in a separate chamber that is differentially pumped by a Varian diode ion pump to a base pressure of $< 1x\ 10^{-8}$ Torr.

A beam of gallium ions is generated from a liquid metal ion source (LMIS) and directed onto a target or substrate using a single lens column. The ions are extracted from a Taylor-Gilbert cone[1] that forms at the end of the LMIS as a result of competing electrostatic stress and surface tension forces. This electrohydrodynamic source emits ions through field evaporation and/or field ionization processes.[2] An example LMIS is shown in Fig. 1.1.

Digital deflection electronics are used to control/switch the octopole voltages used for steering the focused ion beam. Pixel dwell times are controlled from 1.0 μsec to several hundred millisec.

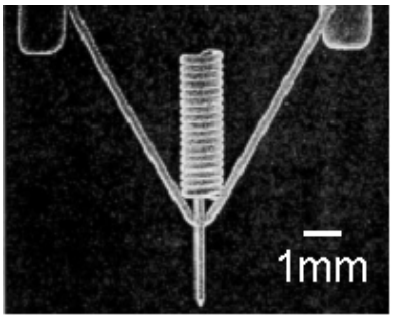

Figure 1.1: Gallium liquid metal ion source from FEI, Co., Hillsboro, OR.

During operation the pressure in our ion beam column may rise to 2 x 10^{-8} Torr or as high as 5 x 10^{-8} Torr when using a gas doser. The ion beam energy is 20 keV for all experiments, and a fixed current of 2.8 nA (measured in a Faraday cup) is selected unless noted otherwise. The beam shape is determined from scanning electron microscopy (SEM) to be roughly Gaussian with a full width at half maximum (FWHM) of 0.6 μm.

A single axis rotary stage attachment allows precise control of sample tilt or rotation if needed. A in-vacuum stepper motor and reduction gear assembly orients a sample through multiple 360^{o} turns if required. Rotation is controlled by a Princeton Research Instruments stepper motor unit using zero holding torque. If a particular, fixed, off-normal angle of incidence is desired, a dial indicator mounted directly on the rotary stage shaft is viewed using the secondary electron detector prior to ion milling. The angle of ion incidence, θ, is defined with respect to the substrate surface normal.

Samples and milled areas are viewed using a channelplate detector. An annular detector (Burle) is used to collect secondary electrons emitted from a bombarded area. This detector is aligned with the ion column and is located just below the column isolation valve as shown in Figure 1.2.

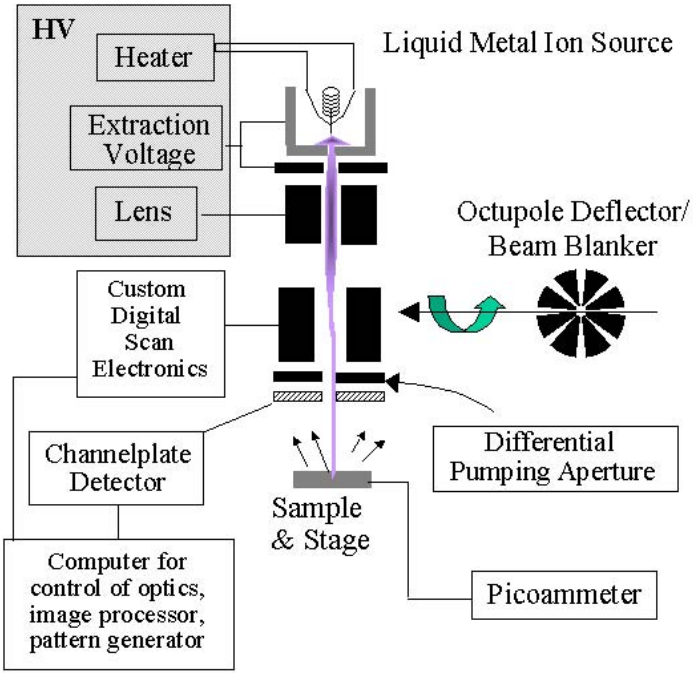

Figure 1.2: Schematic of single lens, focused ion beam system used in this study.

Gas assisted sputtering and chemical vapor deposition (CVD) involves positioning a 250 μm inner diameter nozzle near the sample surface. An optical microscope is mounted on the outside of the vacuum target chamber to check gasjet-sample alignment and to fix working distance (WD) at 250 μm for all gas assisted ion experiments. A 250 μm WD is typical for experiments, because the effects of the assist gas are optimized when positioning the gasjet to a distance approximately equal to the nozzle inner diameter. Gas pressure is manually controlled by an ultra-high vacuum leak valve mounted between a bakeable, stainless steel manifold and the gasjet inlet. A MKS Instruments capacitance manometer gauge (type 628B) indicates pressure between the leak valve and gasjet during operation. This along with an ion gauge measurement of pressure in the target chamber are referenced in this document for gas assisted ion milling and CVD growth experiments.

1.2. References

1 R.G. Forbes, Vacuum, 48. 85 (1996).

2 J. Orloff, M. Utlaut and L. Swanson in High Resolution Focused Ion Beams: FIB and Its Applications (Kluwer Academic, 2003).

Chapter 2. Focused Ion Beam Shaped Microtools for Ultra-Precision Machining of Cylindrical Components

Abstract

Focused ion beam (FIB) sputtering is used to shape a variety of cutting tools with dimensions in the 15-100 μm range and cutting edge radii of curvature of 40 nm or less. The shape of each microtool is controlled to a pre-specified geometry that includes rake and relief features. We demonstrate tools having rectangular, triangular, and other complex-shaped face designs. A double-triangle tip on one tool is unique and demonstrates the versatility of the fabrication process. The focused ion beam technique allows observation of the tool during fabrication, and, thus, reproducible features are generated with sub-micron precision. Tools are made from tungsten carbide, high-speed tool steel, and single crystal diamond. Application of FIB-shaped tools in ultra-precision micro-grooving tests shows that the cross-section of a machined groove is an excellent replication of the microtool face. Microgrooves on 40 μm to 150 μm pitch are cut into 3 mm diameter polymer rods, for groove arc lengths greater than 12 cm. The surface finish of machined features is also reported; groove roughness, R_a, is typically less than 0.2 μm. Ultra-precision machining of cylindrical substrates is extended to make bound metal microcoils having feature sizes of 20-40 μm.

2.1 Introduction

Fabrication of microscale components with cylindrical symmetry is a significant challenge for prototyping and manufacturing. This is particularly difficult when using techniques that generate planar features, such as projection lithography.

Recent work, however, demonstrates processes that overcome some of the geometric limitations of conventional methods. Electronic devices are fabricated onto silicon substrates, such as spheres, using nontraditional lithographic techniques.[1] Microcontact printing on cylindrical surfaces with subsequent electrodeposition produces miniature three-dimensional structures with sub-micron resolution[2], and designed departures from the initial cylindrical geometry.[3] Serial processes such as laser chemical vapor deposition (CVD) [4] are used to deposit free-form helices from organic precursors, and laser stimulated exposure of resist-coated nonplanar substrates is also reported.[5]

Despite progress with these recently-developed techniques, many nonplanar geometries remain difficult to pattern. In particular, fabrication of cylindrical microscale components that have curved or nonrectilinear cross-section features is challenging. This includes, for example, helical threads on a cylinder that have triangular or trapezoidal feature cross sections. Applications that require these geometries include micro-screw components and precisely-shaped knurling tools. Furthermore, most microfabrication techniques (e.g., electroplating, CVD) are capable of patterning a select group of materials. Cylindrical components and devices require a diverse set of materials, including metals, alloys, polymers and ceramics.

Ultra-precision machining techniques are capable of producing microscale structures with complex topology.[6,7] In particular, precision lathe machining is well-suited to cylindrical substrates or components, and many commercial instruments have nanometer-scale precision. However, one of the major difficulties with extending machining processes into the micron range (regardless of workpiece geometry) is the reliable fabrication of small cutting tools with the appropriate shape and dimensions.[8] Lu and Yoneyama[9] describe a micro turning system and emphasize the need for miniaturization of cutting tools in order to achieve the potential of the micro lathe. These authors adapt a diamond scanning probe microscope tip as the cutting tool, while others rely on standard diamond tools[10-12].

Other issues that arise with regard to the widespread applicability of ultra-precision machining using extremely small cutting tools include: the accuracy by which a microtool shape is transferred to the workpiece, the effects of friction/wear on a microtool, the strength and toughness of micron-size tools, the resultant polish of the machined feature (including debris) and the practical limits of feature size, pitch and workpiece diameter.

Focused ion beam (FIB) sputtering is currently being researched as a method for fabricating microscopic cutting tools[13-18] with working dimensions in the tens of micron range. The use of these tools for machining metals, polymers and ceramics is demonstrated in limited tests [16-18] with micromilling and with ultra-precision lathe turning. Development of machining techniques such as establishing the point of contact between the tool and workpiece, and determining reference positions also requires novel procedures, however these are not as challenging as tool shaping. The major advantages to the FIB manufacture of microtools include: the variety of tool shapes, the control over tool geometry, the sub-micron dimensional resolution, and the observation of a tool during shaping. FIB sputtering

creates tool shapes that cannot be fabricated easily by conventional techniques such as polishing and grinding. Also, this technique is beneficial for shaping tools, because negligible mechanical force is placed on the tool during FIB fabrication. Tools are shaped by an atom-by-atom removal process.

This chapter is concerned with cutting tools for ultra-precision lathe turning of grooves on cylinders or other rotationally symmetric shapes. The object is to transfer the tool face shape to the workpiece. The immediate applications include extremely small solenoids and the rotary element of a micro-screw pump. Microcoils and micro-solenoids are good examples of a structure type that is characteristically hard to produce by classical methods. A process consisting of machining (to define features) and metal deposition has the potential to produce small diameter solenoids with a large number of turns per unit length. Small solenoids have proven very tedious to manufacture by winding techniques, particularly for conductor diameters of 25 μm.

2.2. Microtool Fabrication by Focused Ion Beam Sputtering

Starting materials for microtool fabrication are commercially supplied, generally in the form of a tapered cylinder attached to a 3.175 mm diameter mandrel. The total length of the tool shank and mandrel is approximately 2.5 cm. High-speed steel and tungsten carbide tool blanks are available from National Jet, Co. as micro-punches. The final 25 to 120 μm length of the shank is uniform at the specified diameter. Tapered single crystal diamond tool blanks are obtained from Microstar, Inc. The final segment of diamond tool blanks is ~150 μm long with an approximate 40 μm square cross-section.

The focused ion beam system used to shape micro-cutting tools is described in detail elsewhere [19,20]. In general, it is a high vacuum apparatus that accelerates and directs ions at a target material. Material is removed by physical sputtering, and the secondary electrons emitted during this process are collected to form an image of the sample. A tool blank is mounted on an X-Y stage having sub-micron motion resolution, and full 360° rotational motion is available to the tool blank with 0.37° increments. Fig. 2.1 illustrates the orientation of a tool blank with respect to the ion beam (indicated by an arrow), and the removal of segments of a cylindrical tool by sputtering. The microtool depicted in Fig. 2.1. has two cutting faces and is modeled for ultra-precision turning applications. The beam used

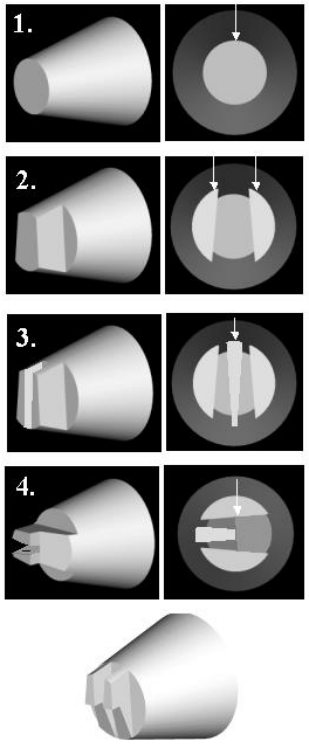

Figure 2.1. Procedure for ion milling (shaping) a micro-threading tool. For all sputter steps, a tool is fixed. Arrows indicate the direction of the ion beam. A completed two-tip design is shown at bottom.

to shape tools is 20 keV, ionized gallium with a spot size of 0.5 μm, and 2 nA total current (as measured in a Faraday cup). The sputter pattern is generated on a bit plane image of the tool end, and can have virtually any shape. This pattern is recorded and transferred to the ion beam deflection system, resulting in a shape in the tool that replicates the pattern. Once all the required facets are ion milled for a given starting rotational position, a tool is rotated to a different orientation, and the process is repeated. Judicious choice of the FIB milling and rotation sequence produces a tool with the target rake angles and extremely sharp cutting edges.

As discussed previously [13-15], a particular ion-solid orientation is used to create sharp cutting edges. With the FIB stage and tool fixed, the gallium beam impinges normal to a plane containing the tool axis. This geometry is ideal for creating one sharp cutting edge per facet on the side furthest from the ion source. The facet edge closest to the ion source is rounded, because a part of the Gaussian beam intensity extends outside the user-defined pattern boundary. In addition, a grazing-incidence geometry employed as a final polish step for each facet minimizes the effects of ion implantation and modifications to tool microstructure, particularly at the far edge of the facet designated for cutting. Transmission electron microscopy reveals that the beam induced changes to tool microstructure are restricted to a 10 nm depth or less when using a 20 keV energy.[21]

The tool materials selected for this study include M42 high-speed steel, C2 grade tungsten carbide, and single crystal diamond. With regard to the FIB fabrication process, the steel and carbide require the smallest time for shaping. A 25 μm wide threading tool made of steel or carbide can be fabricated in 3-5 hours using a 2.0 nAmp ion beam. Note, use of a commercial 20 nAmp ion source would reduce the fabrication time to less than 30

minutes for most tool geometries described in this report. Diamond, on the other hand, requires significantly longer time owing to a relatively high C-C surface binding energy. Despite the slow rate of shaping, we pursue processes that sculpt diamond because these tools are compositionally homogeneous. It is expected that homogeneous materials could be shaped to extremely small dimensions and maintain suitable mechanical properties required for cutting, compared with particular grades of cemented carbide and steels that have relatively large microstructural features and are inhomogeneous.

All three tool materials have several similar characteristics when shaped by focused ion beams. Characteristic features analyzed include the cutting edge radius of curvature, the cutting edge roughness, the facet roughness, and the taper angle formed behind a cutting edge for different tool materials. A summary of focused ion beam-shaped microtool features is presented in Table 2.1.

Tool material	Cutting edge radius of curvature (nm)	Cutting edge roughness, PV(μm), R_a (μm)	Facet roughness, R_{rms}, R_a (μm)	Taper angle of a single facet created by ion beam (degrees)
C2 WC: Co	40	0.15, 0.05	0.14, 0.04	3.0
M42 HSS	n/m	0.11, 0.05	0.13, 0.05	4.1
Diamond	40	0.12, 0.04	0.15, 0.09	2.0

Table 2.1. Metrology of focused ion beam shaped microtools prior to ultra-precision machining. HSS = high-speed steel. WC:Co = cemented tungsten carbide. PV is the peak-to-valley height, R_a is the roughness average and R_{rms} is the root-mean-square average.

In general, the tool cutting edges are extremely sharp. We measure the cutting edge radii of curvature to be 40 nm for diamond and tungsten carbide. Measurements of cutting edge radii of curvature involve initially sputtering two facets onto a tool blank using the FIB system. The two facets are oriented so that they intersect along an edge. The edge of

intersection is then cross-sectioned by a second FIB system and viewed at a magnification of 200,000x in a field emission scanning electron microscope to determine radius of curvature. A representative scanning electron micrograph of a diamond cutting edge is shown in Fig. 2.2. Care is taken to prevent the specimen preparation procedure from affecting the measurement.[22]

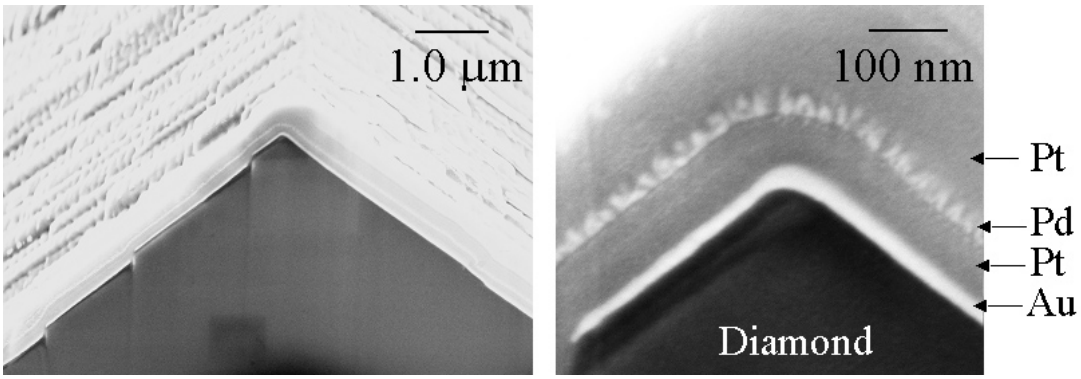

Figure 2.2. Scanning electron microscope images of a diamond microtool cutting edge. The edge is formed by focused ion beam sputtering two facets at a relative angle of ~ 100°. The lower magnification image (left) shows a perspective view of the edge of intersection and a portion of the ion beam milled facets. Several metal layers are also shown in the cross section image on right. These protect the diamond during sample thinning and make the sample conductive for SEM.

In addition to extremely small cutting edge radii of curvature, all tools have a small cutting edge roughness as determined from scanning electron microscopy (SEM). Using SEM we obtain an image of the edge joining two FIB sputtered facets by viewing perpendicular to the edge of interest. Afterwards, SEM micrographs are scanned by a microdensitometer, and the fluctuations in height are analyzed to determine a line roughness. In general, all tool materials show a cutting edge roughness, R_a, of 0.05 μm or less. The peak-to-valley heights along edges are listed in Table 1 and are less than or equal to 0.15 μm.

Facet roughness is also measured for each tool material, and, not surprisingly, this is similar in magnitude to the cutting edge roughness. A calibrated ADE Phase Shift MicroXAM white light interferometric microscope having a vertical (height) resolution of 0.8 Angstroms is used to quantify facet roughness. In general, the R_a of FIB-sputtered facets is 0.04-0.09 μm when measurements are taken away from the facet edges. The facet roughness values listed in Table 1 are comparable with measurements taken from the tools shown in Figs. 2.3-2.5. Facets are extremely smooth but have noticeable nanometer-size steps and ripples that form across the surface when viewed at high magnification using SEM.

When shaping a microtool by FIB sputtering, it is important to recognize that each facet sputtered onto a cylindrical tool blank has a normal direction that is not perpendicular to the ion beam vector. In other words facets are tapered, as shown in Fig. 2.1. Typically facets are oriented 2-4^{o} with respect to the ion beam depending on the tool material (see Table 2.1). The taper angle formed is a result of the physics of the ion-solid interaction. Specifically, ions impinging at near glancing angles most often reflect without displacing atoms from lattice sites. The taper angle resulting from focused ion beam shaping is measured by viewing down the axis of a 25 μm wide tool using SEM. Tools used for this measurement have two nonintersecting facets that are sputtered using a single tool orientation (as shown in Fig. 2.1., step 2). The taper angle generated by the FIB process is measured for each tool material, so that a tool's relief and side rake angles can be tailored to within ~0.5^{o} by the operator. With our FIB system, the stage can rotate a tool to a different orientation prior to sputtering of individual facets.

2.3 Diamond microtools

A micro lathe tool that has been ion milled from a diamond tool blank is shown in Fig. 2.3. The starting material is a single crystal segment that is brazed into a tapered tungsten carbide mandrel, and ground to an approximate 40 x 40 μm square cross section. The width of the tool after ion shaping is 23 μm. A cutting edge formed by the intersection of two ion-milled facets is shown at higher magnification in Fig. 2.3(c). This edge has a roughness, R_a, of 0.04 μm and a radius of curvature equal to 40 nm. The shingled appearance of the FIB-sputtered diamond surfaces shown in Figs. 2.3(b) and (c) is composed of nanometer-size microfacets that form as a result of ion beam bombardment at near-grazing incidence angles. We expect that these features form as a result of a well-documented sputter-induced morphological instability [23] and related phenomena [24].

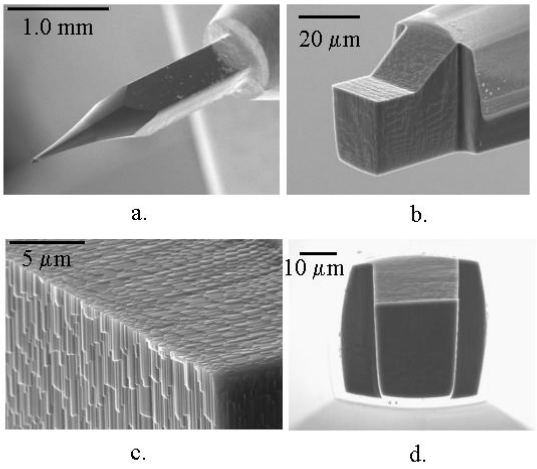

Figure 2.3. (a) Low magnification view of a single crystal diamond tool shank and junction with mandrel. The tool cutting edges are fabricated on the last ~30 μm near the tip. (b) Perspective-view, high magnification scanning electron micrograph of the same diamond tool showing the focused ion beam shaped facets. (c) Left side cutting edge of same microtool. This image shows the intersection of multiple FIB-sputtered facets. (d) End view of the tool.

The end view of the diamond tool is shown in Fig. 2.3(d). This tool is made to have a small side rake angle (2.0^{o}) and relief behind all cutting edges. The fact that the material is single crystal diamond has little effect on the final geometry of the tool; however, the ion-milling rate is significantly lower than that for steel or tungsten carbide as described previously.

Figure 4 demonstrates the ability to tailor tool geometry by the FIB fabrication process. The tool shown in Fig. 2.4 is also shaped from a single crystal diamond blank, but the ion milling patterns and sequences are chosen so that two rectangular cutting surfaces with 10 μm wide tips separated by 7.7 μm result. In general, any complex tool face geometry is possible.

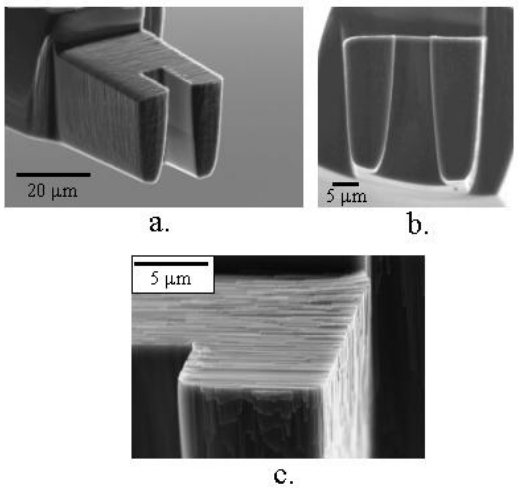

Figure 2.4: (a) Two tip, single crystal diamond tool shaped by focused ion beam sputtering. (b) End view of the same tool demonstrating relief behind cutting edges. (c) High magnification view of a single tip of this two tip tool.

Each of the tips on the tool shown in Fig. 2.4 measure 10 μm wide by 12 μm long. The right tip in Fig. 2.4(b) is 29 μm thick, while the left tip is 26.5 μm thick. The variation

in thickness is a result of the original cross-section of the tool blank, and its orientation to the ion beam. Nevertheless, relief is established behind all cutting edges on this two-tip tool. It is expected that shaping of similar two-tip diamond tools on this scale would be virtually impossible by conventional methods such as grinding.

2.4 Specialized High Speed Steel Tools

Two tool sizes are selected for making high-speed steel lathe cutting tools for different applications. The first application is the production of a cylinder with relatively wide rectangular cross-section grooves. The second application is the production of an ultra-fine triangular groove pair on a cylinder.

Rectangular cross-section grooves

The rectangular cross-section grooves for the first application are large, having a 95 μm width, a 45 μm depth, and a 150 μm pitch. A set of tool blanks that are custom ground to dimensions slightly larger than the final tool size is obtained, and the cutting edges and the rake angles are finished by FIB. The result of shaping a custom ground tool by FIB is shown in Fig. 2.5(a) and Fig 2.5(b). The new sidewalls are separated by 94.9 μm for a length of 70 μm, and the cutting edges have a relief angle of 4.2^{o}. The tool-end cutting edge is also sharpened by ion milling, and a rake facet is defined by FIB.

The tool shown in Fig 2.5 is measured for the sharpness of the cutting edges prior to machining. The cutting edge radii are less than one micron, as determined by scanning electron microscope views at a magnification of 200,000x.

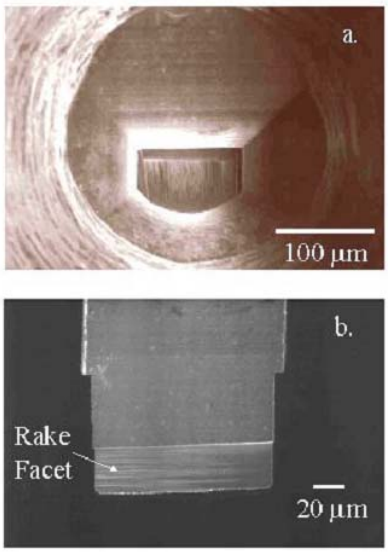

Figure 2.5: Custom ground tool after shaping by ion sputtering. Images show a view along the tool axis (a) and perpendicular to the tool face (b). Ions are used to define sharp cutting edges, relief and a rake facet.

Each custom-ground tool shaped by FIB cut one or more helical grooves in polyether etherketone (PEEK) cylinders. A portion of a PEEK cylinder is mounted in the chuck of an ultra-precision PreciTech lathe (Optimum 2000), with one free end. Each PEEK cylinder surface is cut true with a commercially supplied diamond tool. After polishing, PEEK workpieces have a 3 mm diameter and a total cylinder length of 2.0 cm. The FIB shaped microtool is then brought towards the workpiece surface, and contact is made with the sample as observed through an optical microscope. Multiple passes are made to achieve the final depth; a typical depth per pass is 2 µm or less. Grooves are cut at 500 rpm rotation, and at a longitudinal travel rate of 1.25 mm/sec. The depth cut per pass and the final depth are programmed prior to operation, and the instrument controls rotational alignment and z-axis positioning to allow for accurate machining of a helix.

Figure 2.6 shows portions of a groove cut in a PEEK cylinder. The groove consists of a long helix with a ring at both ends. Each ring is cut to the depth of the helix. The helical portion of the groove begins at a distance of 2.55 mm from the lathe chuck. A portion of the helix is shown in Fig. 2.6(b), demonstrating smooth groove bottom and sidewall surfaces.

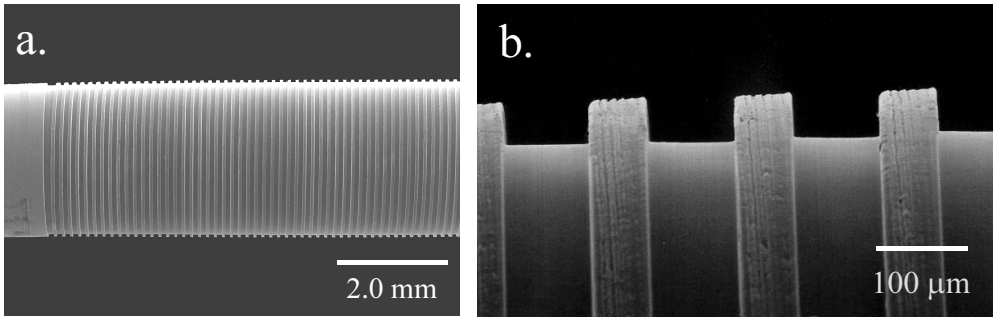

Figure 2.6: Groove machined in PEEK using focused ion beam-polished, custom ground lathe tool. (a) shows an image of the groove ending in a circumferential ring. (b) shows a high magnification view of the smooth helical feature.

We find that for 3 mm diameter PEEK rods cut by tools such as the one shown in Fig. 2.5, the groove dimensions are close to the intended values. Measurements of groove depth, width and pitch are made over arclengths of 225 mm, corresponding to a cylinder length of 3.8 mm. Metrology using SEM includes four measurements on each helical turn, taken in 90^{o} increments. In summary, we find that the width of the helical groove shown in Fig. 2.6 is 94.6 μm with a standard deviation of 0.63 μm. The groove depth is 44.6 μm with a standard deviation of 2.3 μm. The roughness of the machined feature bottom is determined by white light interferometry to be 0.22 μm (R_{rms}) and 0.14 μm (R_a). A table at the end of this paper summarizes results from all ultra-precision machining tests using FIB-shaped tools.

Beyond cylinder lengths of ~ 4.0 mm the FIB-polished microtool significantly deflects the workpiece, and as a result the groove depth deviates by $\geq$10% of the intended value. Evidence of a rough surface finish created during a polish step can also be found at these lengths, most likely due to chatter. It is expected that grooves of constant depth can be made substantially longer by using a tail stock for workpiece support.

Two PEEK cylinders are cut with the tool shown in Fig. 2.5, and the material volume removed from each is 4.5×10^{-3} cm^3. The tool edges are inspected after cutting each PEEK cylinder to ensure that the tool remained sharp. The tool cutting edge radii increased no more than 0.1 μm after the second grooving operation.

Double triangle grooves

The second application of high-speed steel tools includes machining a pair of closely spaced triangular grooves into the surface of a 3-mm diameter PEEK rod using a two-tip tool. This tests both the ability of FIB to make a two tip tool having a nonrectilinear tool face shape and the ability of a lathe machine to position a microtool along the z-axis of the cylinder and to maintain rotational alignment. Ultra-precision machining with this tool involves multiple passes, whereby the tool is reengaged several times at the origin of cut.

Figure 2.7 shows two views of a high-speed steel two-tip tool, before lathe machining. Each tip face is triangular and has an included angle of 62.5^o as shown in Fig. 2.7.b. A back rake angle of 10^o is also created for both tips. A relief angle of approximately 4^o is established behind all cutting edges and behind the two end points of the tool. The two tips are 24 μm long.

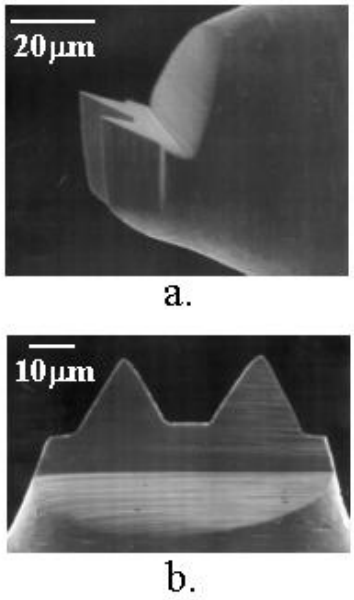

Figure 2.7: Two-tip microtool having triangular cutting faces. Tool is made of M42 high speed steel and is shaped by focused ion beam sputtering. Image in (b.) shows the cutting face.

Figure 2.8 shows a portion of the triangular grooves cut into 3 mm diameter PEEK rod using the tool shown in Fig. 2.7. Qualitatively the tool shape appears to be replicated very well in the cross-section of the grooves indicating that the Optimum 2000 lathe does an excellent job of managing rotational alignment and z-axis control. Both grooves in Fig. 2.8. have an angle of approximately 62.5°. The depths of the two grooves are also similar and close to the intended depths, ~ 15 μm. The pitch of the groove pair is 150 μm, and the total arc length of each groove is 18 cm.

Measuring both the groove angle and the groove depth as a function of arclength has made a more stringent evaluation possible. Figure 2.9 shows the measurements of depth and angle at the beginning of a helix, and after numerous turns. This includes measurements made at 90^{o} increments per helical turn. In general, Fig. 2.9 demonstrates

that both the angle and depth are virtually independent of rotational position around the circumference. This consistency owes to the precision of the machine, the ability to make a workpiece round on the lathe prior to groove definition, and the lack of workpiece deflection by the FIB-shaped microtool for large cylinder lengths. This particular tool leads to far less workpiece deflection than the larger tool shown in Fig. 2.5, and no change in groove depth is observed along the entire machined cylinder length.

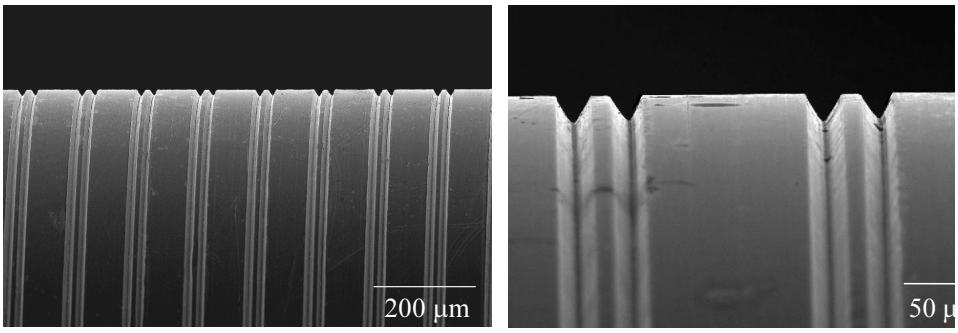

Figure 2.8: A portion of the PEEK workpiece machined using the focused ion beam shaped, two-tip tool shown in Fig. 2.7.

In Table 2.2, we summarize the characteristics of several lathe machined grooves. In general, there is excellent matching between the target groove dimensions and the measured values. The widths and cross sectional shapes of the machined features are nearly identical to that of the microtool face as evaluated using SEM. This matching continues for many turns along the cylindrical workpieces. The groove arclengths listed are those over which the features remained uniform and, in some cases, the total length. However, there is reason to expect that uniform features could be machined to much greater lengths with workpiece support.

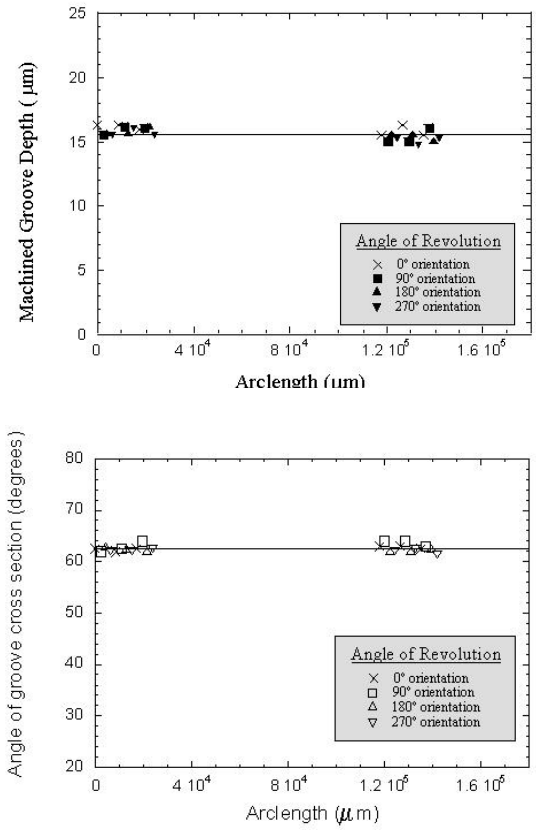

Figure 2.9. Plots of (a.) machined groove depth and (b.) groove cross section angle. Data is obtained from an ultra-precision machined PEEK cylinder and is plotted as a function of the groove arclength for different workpiece rotation quadrants.

Tool dimensions, groove widths and groove depths are measured using SEM. In order to determine groove dimensions, the workpiece is positioned so that the cross-section of a groove can be viewed. Multiple turns are analyzed to determine average depth and width including measurements for different quadrants of rotation. A calibrated ADE Phase Shift MicroXAM white light interferometric microscope is used for measurements of groove roughness for those helical features having a rectangular cross section. As mentioned previously, this instrument has a vertical (height) resolution of 0.8 Angstroms in

the mode used for analysis. Workpiece cylindricalness is removed to allow for an accurate determination of roughness along the groove bottom. PEEK samples are insufficiently reflective for measurement by the interferometer. These require a thin layer (~15 nm) of Au/Pd.

Workpiece Material {diameter, mm}	Groove length, mm	Tool face shape	Tool face angle, degrees	Groove angle {st dev}, degrees	Tool width, μm	Groove width {st dev}, μm	Target Depth, μm	Groove depth {st dev}, μm	Groove roughness R_{rms} ; R_a , μm
PEEK {3.00}	225	Rectangle	90	90 {0.4}	94.9	94.6 {0.63}	45.0	44.6 {2.3}	0.22 , 0.14
PEEK {3.00}	219	Rectangle	90	90 {0.4}	92.9	92.1 {0.5}	45.0	45.7 {1.4}	0.16 , 0.13
Cu /PMMA {3.00}	377	Rectangle	90	90 {0.2}	19.0	19.3 {0.2}	15.0	15.2 {0.5}	0.25, 0.20
PEEK {3.00}	140	Triangle	62.5	62.65 {0.49}	20.0	19.9 {0.1}	15.5	15.67{0.47}	N/M
PEEK {3.00}	140	Triangle	62.5	63.10 {0.80}	18.4	18.5 {0.1}	14.0	14.25{0.54}	N/M

Table 2.2. Results from threading different workpieces with focused ion beam shaped microtools. Tool width for the triangular shaped microtools is defined as the width of the tool face at a distance from the tool end equal to the target groove depth. Roughness is measured on the bottom of a machined groove. N/M = not measured.

2.5. Fabrication of miniature solenoids

Miniature electric windings or solenoids formed on cylinders of 3 mm diameter or less with conductor cross-section dimensions on the order of 25 μm are extremely painstaking to fabricate by hand wrapping and have low yield. Therefore, a variety of processes are being investigated to make high winding density microcoils for use as magnetic actuators, transformers, and sensors [25-28]. Processes researched to date include soft lithography [27], LIGA [29], wire wrapping by automated devices [30], and chemical vapor deposition [4].

In this report, we describe two different processes for fabricating microcoil structures that could find use in prototyping or small-lot production. These processes take

advantage of the FIB tool shaping and the precise lathe micromachining techniques described in previous sections. We combine these ultra-precision machining techniques with thin film vapor deposition and electroplating.

The first process involves coating a cylindrical-shaped polymer such as polymethyl methacrylate (PMMA) or PEEK. As an example, we use a 20 μm thick Cu conducting layer that is deposited by electron beam evaporation and subsequent electroplating. A FIB shaped tool is then employed in a precision lathe to cut the conductive layer in sequentially increasing depths until the (soft) insulating support is reached. The result is an electrically isolated helical winding in which the conductor width is determined by the pitch of the micro-turning operation. The thickness of the metal conductor is set by the electroplating procedure and etching (if removal of debris is deemed necessary). Areas at both ends of a helical cut serve as rigid contact cuffs for wire bonding.

Figure 2.10 shows the helical cut in a copper coating on a 3.0 mm diameter PMMA rod. This helix has a pitch of 74 μm, leaving a conductor with a rectangular cross-section of 45 μm by 15 μm. Samples can be cleaned to remove debris by brushing or etching.

The second coil fabrication method is essentially an adaptation of the Damascene [31] process used on planar substrates for microelectronics. In our experiments, a 1.0 mm diameter Macor rod is chosen as the insulating substrate, and 20 μm wide grooves are

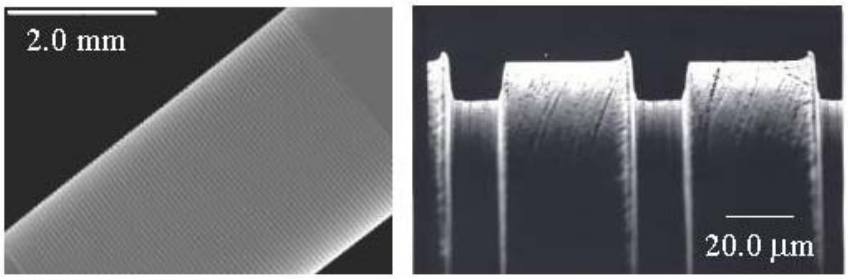

Figure 2.10. Images of a single thin film coil bound to a PMMA cylindrical substrate. Component is made by depositing a Cu film followed by ultra-precision lathe machining.

machined into the surface using a FIB-made tool to a depth of 20 μm, with a pitch of 70 μm. The repeated pattern consists of five helical turns as shown in Fig. 2.11a. The substrate is then coated with vacuum evaporated Cr to promote adhesion followed by a seed layer of Cu. Subsequently the sample is electroplated with Cu to a thickness that exceeded the original diameter of the Macor cylinder. A mechanical polish removes the excess copper until the underlying Macor support is exposed. The result, shown in Fig. 2.11b, is electroplated copper windings contained on a machined Macor cylinder, with each conducting path separated by insulating ceramic. Helical segments shown in Fig 2.11. are separated by 200 μm long copper contact areas (cuffs). These are areas machined during the same ultra-precision lathe turning process. Metal films are plated into these areas for the purpose of wire bonding.

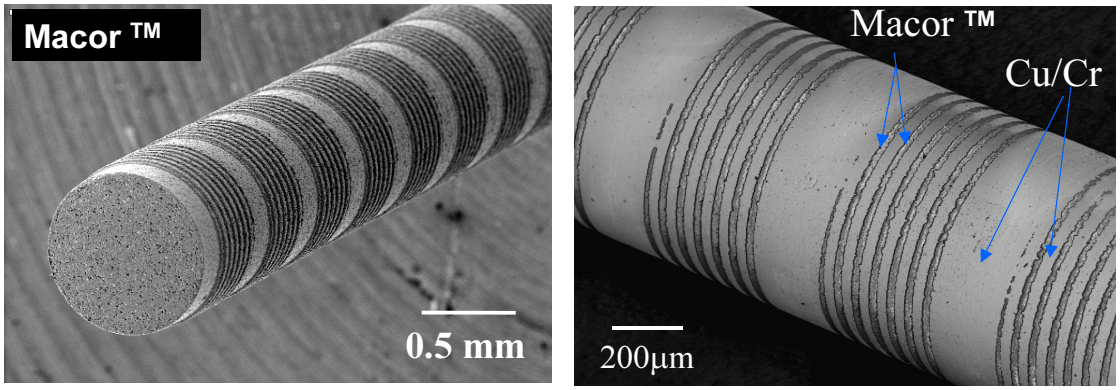

Figure 2.11. Two stages of the Damascene process used to make thin film microcoils Helical grooves are patterned by ultra-precision machining as shown in (a.). Afterwards, Cr / Cu seed layers are deposited, and electroplating is used to thicken the metal. Polishing after deposition and plating results in a completed microcoil shown in (b.).

2.6. Summary and future work

This work successfully extends conventional lathe machining techniques to the microscale in order to fabricate a variety of cylindrical components. In general, we demonstrate methods that allow for control of feature cross-section. This includes the ability to tailor nonrectilinear feature shapes uniformly around the circumference of a workpiece.

Focused ion beam sputtering is used to precisely shape micro-threading tools that have well-defined back and side rake angles, cutting edge widths and relief. A particular ion beam – sample orientation used during microtool shaping is responsible for generating extremely sharp cutting edges. This orientation is particularly useful for shaping edges in compositionally inhomogeneous materials such as cemented carbide and tool steel. The cutting edge roughness of M42 high speed tool steel, diamond and C2 tungsten carbide tools

is measured to be 0.05 μm or less. The cutting edge radius of curvature is also a small fraction of the microtool width and length, making the cutting edge sharp compared to the depth per pass used during machining (typically 2 μm in this study). Scanning electron microscopy reveals that tools have cutting edge radii of curvature equal to 40 nm or less.

Focused ion beam sputtering has the advantage that almost any conceivable microtool geometry can be fabricated on a scale that is below those reached by grinding methods. This includes the potential fabrication of tools with curved shapes. We demonstrate the advantages of FIB sputtering in this paper by showing microtools with multiple tips separated by small gaps. Tools with nonrectilinear face shapes are shown including triangular tools. These tools are subsequently used to define features on cylindrical components by ultra-precision machining. In general, machined feature cross-sections closely match tool face shape. Metrology of machined workpieces shows nearly identical feature widths and included angles compared with the fabricated microtools. Measurements of groove depth around the circumference of cylindrical workpieces show good matching independent of arclength, thus demonstrating the ability of precision lathe machines to fabricate microscale and miniature cylindrical components. Additional work takes advantage of the ability to define a precise helix and fabricates thin film microcoils with 25 μm wide metal turns.

Although FIB sputtering is a relatively slow process compared with other techniques, we envision that a high yield tool-making process with reasonable throughput can be achieved using existing focused ion beam technology. FIB sputtering imposes no large forces on the tool during fabrication; material is removed atom by atom. Therefore, it is unlikely that a tool will be broken during fabrication. In terms of the time required for

fabrication, a focused ion beam column capable of producing 20 nAmp current (compared with our 2 nAmp beam) would allow for fabrication of a 25 μm wide high speed steel and tungsten carbide tool in less than 30 minutes.

Diamond cutting tools shaped by focused ion beam sputtering are also demonstrated in this report with extremely precise dimensions and complex tool face shapes, but greater fabrication times are required compared with the other two materials studied. In general, a diamond tool can be made to have rake, relief, minimal cutting edge roughness and an extremely small radius of curvature (~ 40 nm or less), but these tools require many hours of sputtering. Nevertheless, recent studies [32] demonstrate a modification to the current technique, known as gas-assisted FIB sputtering, that should reduce the required time to shape a tool. Based on known effects of H_2O-assisted sputtering [33] of diamond, it is reasonable to expect that our process for shaping a 25 μm wide diamond tool can be modified to relatively short time (30 minutes or less) when using a 20 nAmp beam. Future research must examine the effects of different rate-enhancing 'assist gases' on microtool cutting edge roughness and radius of curvature.

2.7. References

1. See examples by Ball Semiconductor, Inc. Allen, Texas 75013.

2. Jackman RJ, Brittain ST, Adams A., Prentiss MG, and Whitesides GM, Design and fabrication of topologically complex, three-dimensional microstructures. Science, 1998; 280:2089-91.

3. Brittain ST, Schueller OJA, Wu HK, Whitesides S, Whitesides GM, Microorigami: Fabrication of Small, Three-Dimensional, Metallic Structures. Journal of Physical Chemistry B 2001; 105(2): 347-350.

4. Maxwell J, Larsson K, Boman M, Hooge P, Williams K, and Coane P, Rapid prototyping of functional three dimensional microsolenoids and electromagnets by high-pressure laser chemical vapor deposition. Proceedings of Solid Freeform Fabrication Symposium1998; 529-36.

5. *see* Trenkel C, Hammond GD, and Speake CC, Photolithographic manufacture of a superconducting levitation coil on a spherical substrate, Prec. Engin., 1999; 24: 139-145. *and* Lullo G, Arnone C, and Giaconia C, Technologies for the fabrication of cylindrical fine line devices. Microelectronic Eng.,1997; 35: 417-20.

6. Weule H, Huntrup V, and Tritschler H, Micro-cutting of steel to meet new requirements in miniaturization. Annals CIRP, 2001; 50: 61.

7. Schaller Th, Bohn L, Mayer K, and Schubert K, Microstructure grooves with a width of less than 50um cut with ground hard metal micro end mills. Precision Engineering 1999; 234: 229-35. T. Schaller and K. Schubert, Micromachining by CNC slotting using a standard tool, ASPE Proc. 2001; 25: 469-477.

8. Hoffmeister H-W, Wenda A, and Herrman H, The fabrication of micro milling cutters, Proc. International Conference on Microtechnologies: Microtec 2000, 25-27 Sept 2000, Hanover Germany;125-29.

9. Lu Z, and Yoneyama T, Micro cutting in the micro lathe turning system. International Journal of Machine Tools and Manufacture, 1999; 39: 1171-1183.

10. Okazaki Y, and Kitahara T, NC Micro-lathe to machine micro-parts. ASPE Proc. 2000; 22: 575-578.

11. Bohart A, Collins P, Faulk S, Halvorson C, McClellean M, and Shillito K, Affordable, compact, research single point diamond turning machine. ASPE Proc. 2000; 22: 184-186..

12. Clarke M, Pierse M, Knuefermann M, and Read R, New technology and novel design make sub-micron production practical. ASPE Proc. 2000; 22: 187.

13. Vasile M, Friedrich C, Kikkeri B, and McElhannon R, Micrometer scale machining: tool fabrication and initial results. Precision Engineering, 1996;19:180-6.

14. Friedrich C, and Vasile M, Development of the micromilling process for high aspect ratio microstructures. J Microelectromech Systems1996;5:33-8.

15. Friedrich,C and Vasile M, Micromilling development and applications for microfabrication. Microelectronic Engineering 1997; 35: 367-72.

16. Adams DP, Vasile M, Benavides G, and Campbell A, Micromilling of metal alloys with focused ion beam-fabricated tools. Precision Engineering 2001;25:107-13.

17. Adams DP, Vasile M, and Krishnan A, Microgrooving and microthreading tools for fabricating curvilinear features. Precision Engineering, 2000;24:347-56.

18. Adams DP, Vasile M, and Picard Y, Focused ion beam shaped micro-cutting tools for fabricating curvilinear features. ASPE Proc. 2000; 22: 176.

19. Harriott L, A second generation focused ion beam micromachining system. Proc SPIE, 1987; 773, 190.

20. Vasile M, Biddick C, and Schwalm S, Microfabrication by ion milling: the lathe technique. Journal of Vacuum Science and Technology B 1994;12, 2388.

21. Adams DP, Mayer TM and Vasile MJ, to be published, 2002.

22. Sample preparation for electron microscopy involved deposition of a protective Au metal film onto the microtool using electron beam evaporation. The sample was then coated with a Pt-C layer by electron beam CVD. Additional layers include Pd (used as a marker) and a relatively thick Pt-C layer deposited by FIB-CVD. The deposited metals protect the tool edge morphology during ion beam thinning and prevent charging in the electron microscope. A single region is sputtered along the edge of intersection using a different focused ion beam sputter system (FEI DB235).

23. Bradley R Mark and Harper James ME, Theory of ripple topography induced by ion bombardment, J. Vac. Sci. Technol. A 1988; 6(4) 2390-2395.

24. G. Carter, The effects of surface ripples on sputtering erosion rates and secondary ion emission yields, J. Appl. Phys., 1999; 85(1), 455-459.

25. Klein J, and Guckel H, High winding density micro coils for magnetic actuators, Microsystem Technologies, 1998; 4, 172-175.

26. Christenson TR, Klein J, and Guckel H, An electromagnetic micro dynamometer, Proc. IEEE MEMS, Amsterdam, Netherlands 1995; 386-391.

27. Rogers JA, Jackman RJ, and Whitesides GM, Constructing Single- and Multiple-Helical Microcoils and Characterizing Their Performance as Components of Microinductors and Microelectromagnets, J. Microelectromech. Syst., 1997; 6 (3), 184-192.

28. Webb AG , Radiofrequency microcoils in magnetic resonance, Progress in Nucl. Magn. Reson. Spectroscopy, 1997, 31, 1-42.

29. LIGA is an acronym for Lithographie-Galvanoformung-Abfromung. see Becker EW, Ehrfeld W, Hagmann P, Maner A and Münchmeyer D, Fabrication of microstructures with high aspect ratios and great structural heights by synchrotron radiation lithography, galvano-forming, and plastic moulding (LIGA process), Microelectron. Eng., 1986; 4, 35-56.

30. Mahdjour H, Clark WG, and Baberschke, High sensitivity broadband microwave spectroscopy with small non-resonant coils, Rev. Sci. Instrum. 1986; 57(6), 1100-1106.

31. Dalal HM, Joshi RV, Rathore HS and Phillipi A, A dual damascene hard metal capped Cu and Al alloy for interconnect wiring of ULSI circuits, Proc. Int. Electron Dev. Mtg., 1993; 273-276.

32. see references in Orloff J, High-resolution focused ion beams, Rev. Sci. Instrum, 1993; 64 (5), 1105-1130.

33. Russell PE, Stark TJ, Griffis DP, Phillips JR, and Jarausch KF, Chemically and geometrically enhanced focused ion beam micromachining, J. Vac. Sci. Technol. B 1998; 16(4) 2494-2498..

Chapter 3. Focused ion beam milling of diamond: Effects of H_2O on yield, surface morphology and microstructure

3.1. Introduction

Focused ion beam (FIB) sputtering[1] is a technique that is currently used to fabricate microdevices and microtools. FIB methods are attractive for prototyping at the microscale, since these can shape almost any solid including hard materials. In addition, focused ion beams are beneficial, because negligible force and heat are imposed on a target during fabrication. Nanoamperes are typically used during focused ion milling, and the range of 10-30 keV ions in solids is small, approximately a few hundred Angstroms. Micron-scale features are precisely shaped with nanometer precision, because current FIB systems maintain a small beam size (5-1000 nm), excellent beam positioning accuracy, large depth of focus and stable operating conditions.[1] When combined with a multi-axis stage having rotation[2], this micromachining technique can be used to sculpt geometrically complex objects. An example 20-micron wide, diamond cutting tool shaped by focused ion beam sputtering is shown in Fig. 3.1.

Processes such as FIB sputtering that fabricate diamond and related materials are of interest for improving micron-scale devices, sensors and instruments.[3-10] Various applications benefit from the use of diamond, because it has a high thermal conductivity, negative electron affinity, and a relatively large band gap. For microtools and indenters, a high yield strength and chemical inertness at low temperature are germane. Diamond has the highest hardness (~100 GPa) of any material found in nature.[11,12]

Despite interest in diamond, processes that shape this material by sputtering suffer from a low removal rate. High energy (20-50 keV), focused ion beam sputtering at normal incidence is characterized by a yield = 0.09 μm^3/nC, corresponding to ~2 atoms/ion.[13-15] Using the maximum current afforded by commercial FIB systems (20 nAmps), diamond can be sculpted at a rate of ~1.8 μm^3/sec. A low sputter rate is attributed to a high C-C surface binding energy equal to 7.5 eV.[16]

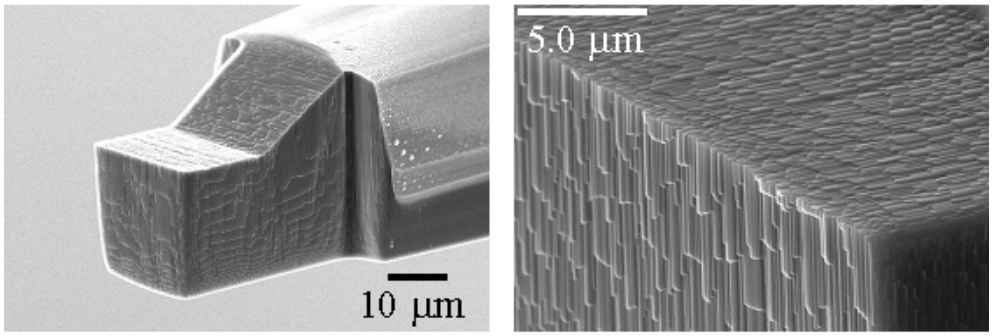

Figure 3.1. Focused ion beam shaped, diamond microtool for ultra-precision lathe turning operations. The tool has cutting edge radii of curvature[3] equal to 40 nm. Image on right shows intersection of three FIB sputtered surfaces at high magnification. All surfaces are created by sputtering near grazing incidence ($\theta \sim 85^o$).

Several advances have been made to improve the 'ion beam machinability' of diamond. A common strategy to enhance the yield of this or other low sputter rate materials involves exposure of the bombarded area to a reactive gas (a process referred to broadly as chemical assisted etching). As described by Harriott,[17] for most applications an ideal chemical assist gas increases the rate of sputter removal, minimizes the effects of redeposition and reduces implantation of the primary ion species in a sample. Previous research shows that a reactive gas can increase the material removal rate by lowering the binding energy of surface species thereby generating volatile etch products, or by changing the dynamics of the ion-generated

collision cascade.[18] Chemical assisted etching processes specific to diamond have been reported by several groups.[13,14,19-22] Early work by Efremow et. al.[19] with Xe^+ ion beams showed a 10x increase in material removal rate when using a reactive flux of NO_2. Russell et. al.[14,20] more recently showed that a less hazardous gas, H_2O, can be used to significantly enhance the rate of diamond milling. Introduction of H_2O during 25keV Ga^+ bombardment of C at $\theta = 0^o$ (normal incidence) led to a 5-11x enhancement in material removal rate compared with similar ion beam processes having no chemical assist.[20,21]

A more complete understanding of H_2O–assisted ion milling is required for tailoring the shape of future diamond instruments. Micro-tools having curved surfaces (e.g., hemisphere) and small surface roughness are of interest for indentation and ultra-precision machining. In order to control curved shapes accurately by FIB, we require knowledge of the material-specific, sputter yield angular dependence, $Y(\theta)$.[23] A FIB technique put forth by Vasile et. al.[24] converts an initially planar surface into predetermined curved shapes in a single mill step. However, this procedure requires knowledge of $Y(\theta)$ when solving numerically for required pixel dwell times. In general, we must determine $Y(\theta)$ for the exact conditions used during FIB processing, including the presence of an assist gas (if used). The surface morphology that develops during FIB milling is also of great importance for diamond applications. For example, the six-sided diamond microtool shown in Fig. 3.1 exhibits a distinct step/terrace morphology on surfaces sputtered at near-grazing incidence angles ($\theta \sim 88^o$). Fabrication of a smooth, highly curved surface can be more difficult as shown in Fig. 3.2 for a microindenter tip. This tool is nominally shaped by FIB sputtering into a hemisphere starting from a flat face on a near-cylindrical blank. By maintaining the scanned beam parallel to the tool axis, a variety of morphological features evolve at different angles

of incidence including: smooth surfaces at $\theta < 40^o$, ripples at $40^o < \theta < 75^o$, and a step/terrace topography at $\theta > 70^o$.

For this study, we analyze yield, surface morphology and changes in microstructure for ion bombardment at different angles of incidence, θ, with and without H_2O assist. High doses, ~10^{18} ions/cm^2, are chosen, because previous work[15] shows that diamond attains a near-constant, normal incidence sputter yield at these values. High dose experiments therefore allow for a meaningful comparison of the two FIB techniques and identification of H_2O-induced effects.

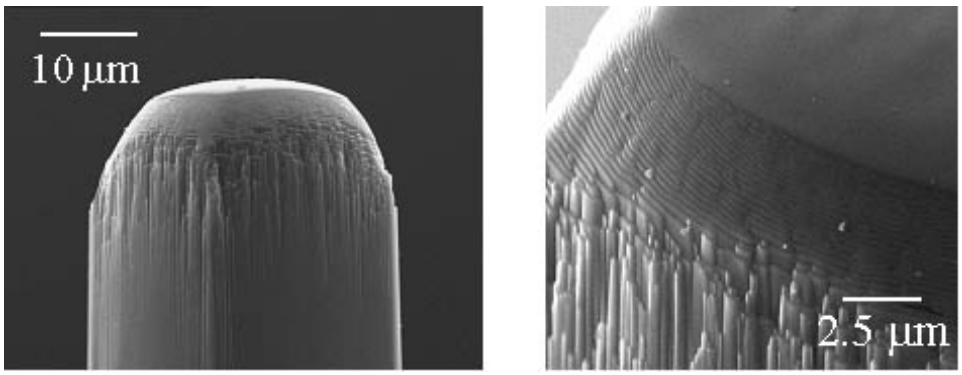

Figure 3.2. Prototype FIB-shaped, single crystal diamond, curved tip microindenter. The focused ion beam is scanned across the stationary tool with the ion beam vector parallel to the tool axis. The pixel dwell time is varied to tailor net shape. On right is a high magnification view of the same tool showing three unique surface morphologies. No assist gas is used.

3.2. Experimental

A custom-built focused ion beam system is used for ion milling experiments as described in Chapter 1.[25] The target chamber has a base pressure of 1 x 10^{-7} Torr and contains a precision x-y stage, a sample cassette, a custom-built gas doser, a secondary

electron detector and a residual gas analyzer. The ion column is located in a separate chamber that is differentially pumped by a Varian diode ion pump to a base pressure of < 1 x 10^{-8} Torr. A beam of gallium ions is generated from a liquid metal ion source (FEI, Inc.) and directed onto the target using a single lens column. During operation the pressure in the ion beam column may rise to 2 x 10^{-8} Torr, or as high as 5 x 10^{-8} Torr when using a H_2O doser. The ion beam energy is 20 keV for all experiments, and a fixed current of 2.8 nAmps (measured in a Faraday cup) is selected. The beam shape is determined by scanning electron microscopy (SEM) to be roughly Gaussian with a full-width at half maximum (FWHM) of 0.6 μm. A single-axis rotary stage attachment allows precise control of sample tilt and, therefore, ion beam incidence angle.[26] An in-vacuum stepper motor and reduction gear assembly can orient a sample through 360° if necessary. Rotation is controlled by a Princeton Research Instruments stepper motor unit. In order to ensure that a particular angle of incidence is selected prior to each mill step, a dial indicator mounted directly onto the rotary stage shaft is viewed using the secondary electron detector. We expect that this arrangement along with procedures for leveling diamond specimens using an interferometric microscope (ADE Phase Shift MicroXAM) reproducibly establish the angle of incidence, θ, with an uncertainty of $\pm$ 0.25°. The angle of ion beam incidence, θ, is defined with respect to the substrate surface normal.

Gas-assisted ion milling involves positioning a 250 μm inner diameter nozzle near the sample surface. An optical microscope is mounted on the outside of the vacuum chamber to check gasjet-sample alignment and fix working distance (WD) at 250 μm for all gas-assisted ion milling experiments (with the exception of the data shown in Fig. 3.3). A 250 μm working distance is chosen, because the effects of H_2O for enhancing yield are

optimized when positioning the gasjet aperture to a distance approximately equal to the nozzle inner diameter. As demonstrated in Fig. 3.3. for experiments at $\theta = 0^{o}$ and a pixel dwell time of 65 μs, the yield is constant for working distances between 100-250 μm, while spacings greater than 250 μm lead to only a slight enhancement compared with FIB sputtering with no H_2O present. Gas pressure is manually controlled by a UHV leak valve mounted between a bakeable, stainless steel manifold and the gasjet inlet. A MKS Instruments capacitance manometer gauge (Type 628B) indicates 7.1 Torr between the leak valve and gasjet during H_2O–assisted experiments. Based on similarities in gasjet-sample geometry with Stark et. al. [21], we estimate that the H_2O pressure at the sample surface is 0.1 Torr when using a WD = 250 μm.

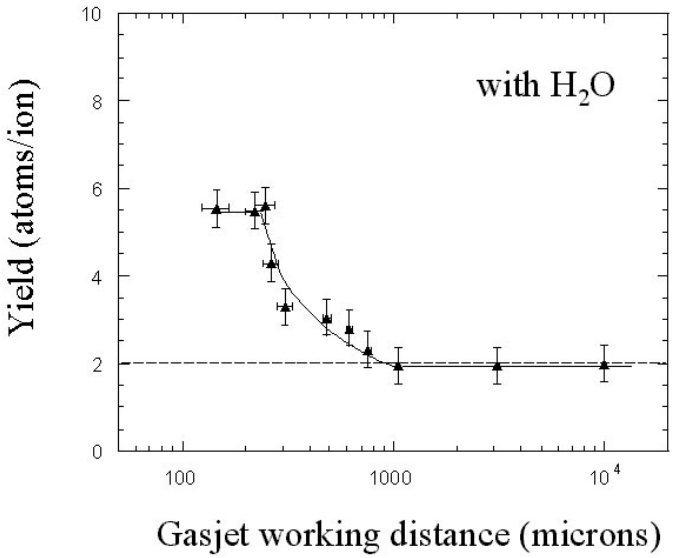

Figure 3.3. Plot of yield (C atoms/ion) as a function of gasjet working distance for H_2O assisted ion milling. Dotted line shows the sputter yield for FIB sputtering with no gas present.

3.3. Results and discussion

Yield of Diamond: FIB sputtering and H_2O-assisted FIB milling

Experiments determine the angular dependence of yield, Y(θ), defined as the number of C atoms removed per incident Ga^+ ion. A clean, smooth[27] specimen of single crystal (100) diamond is first mounted and leveled to the plane of the cassette. Once inserted into the vacuum chamber, a sample is tilted to a particular angle, viewed, and bombarded within targeted areas. Our FIB milling procedure involves outlining a square box feature and exposing the area to a focused gallium beam. For experiments at $\theta \leq 80^o$, 12 x 12 μm boxes are outlined as viewed in projection by the operator. This 62 x 62 pixel box defines the area of the diamond surface over which the beam is rastered equal to $12x12/\cos\theta$ (μm^2). Experiments at angles greater than 80^o require 12 x 6 μm boxes (area = $12x6/\cos\theta$ (μm^2)), because the feature becomes extremely long in one direction. Outlining a box with a reduced y dimension shortens the feature allowing for accurate measurements of sputtered volume after removal from the vacuum system. In addition, H_2O-assist experiments at high θ require a reduced feature length in order to maintain a constant gas pressure across the exposed area. Experiments are designed to keep the ion-milled feature less than 200 μm long when using the 250 μm inner diameter gasjet. Yields are determined at different ion beam incidence angles, typically in 5^o increments. For FIB sputtering experiments, we are also able to measure yield at extremely high angles of $\theta = 86$, 87, 88 and 89^o. In all cases, the focused ion beam is scanned across the area of interest in a serpentine pattern. Despite rastering, a uniform ion dose is given to each outlined area. The near Gaussian shaped, 0.6

μm-FWHM ion beam is relatively large compared with the pixel spacing of 0.19 μm, thus, providing substantial beam overlap.

Fig.3.4 shows a plot of the measured yield versus ion beam incidence angle for both FIB sputtering and H_2O-assisted FIB milling processes. For these experiments, we use a pixel dwell time of 130 μs and a refresh time[28] of 351.98 msec. Yield is determined after

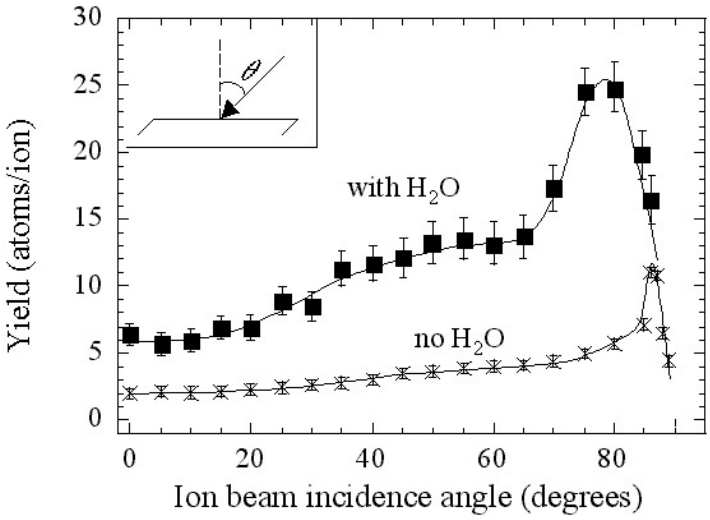

Figure 3.4. Plot of yield (C atoms/ ion) versus ion beam incidence angle, θ. Two data sets are shown including results from gallium ion beam bombardment (x) and H_2O-assisted processes (■). The lines shown are guides to the eye. θ is defined with respect to the substrate normal as shown in the inset.

removing the sample from the vacuum system. Sputtered volume is first measured using a calibrated ADE Phase Shift MicroXAM interferometric microscope having 1 Å vertical resolution. Interferometry accurately determines milled feature volume; feature depths measured by this technique are nearly identical to those measured by a calibrated atomic force microscope. The yield is equal to $1.602 \times 10^{-19} \times \rho \times V_c / (i_{Ga} \times t)$ where ρ is the density

of diamond[29] (1.76 x 10^{11} atoms/μm^3), V_c is the sputtered cavity volume, i_{Ga} is the beam current measured in a Faraday cup, and t is the exposure time. We expect the yields determined assuming a density of single crystal diamond are not greatly affected by a known ion-induced change in crystal structure of the near-surface region. Although transmission electron microscopy shows that the carbon substrate is amorphized to a depth of 10-50 nm (demonstrated later in this report), this thickness is relatively small compared with the feature depth.

FIB sputter yield depends on ion beam incidence angle with the lowest material removal rates occurring at 0^o and near 90^o. For FIB sputtering, we find $Y(0^o)$ equals 2.0 consistent with previous works.[13-15,21] There is a slight increase in sputter yield between 0 and 80^o followed by a sharp rise between 80 and 85^o. A maximum yield, Y_{max}, is found at 86^o. The angle at which $Y_{max}(\theta)$ occurs is in good agreement with TRIM calculations.[30] These simulations confirm that the FIB sputter yield peaks at angles greater than 80^o due to the deeply penetrating nature of the high-energy ion beam. Experiments demonstrate a decreased FIB sputter yield for angles greater than 86^o. This presumably occurs because of ion reflection. A Ga^+ ion will reflect off a smooth surface with higher probability as the angle of incidence approaches 90^o. We do not expect redeposition of ejecta complicates our measurements of volume and calculations of FIB sputter yield. The largest FIB sputtered feature depth is 3.65 μm. Therefore, the depth/width aspect ratio of sputtered features is 0.30 or less.

The yield characteristic of H_2O-assisted FIB milling is also dependent on ion beam incidence angle but shows a broader peak at high angles compared with FIB sputtering. The milling yield at 0^o is 6.4 atoms/ion, and an increase is found with angle up to $\theta = 75^o$. For

H_2O-assisted milling, the peak yield (25 atoms/ion) occurs at an angle ~ 75-80°. Note, the angle for which $Y(\theta) = Y_{max}$ is less than that for FIB sputtering with no gas assist.

For all angles of incidence probed in this study, H_2O leads to an increased yield compared with FIB sputtering and no gas assist. When using a pixel dwell time of 130 μs, the yield is enhanced 1.5-4.8x for angles in the range 0-86°. The amount by which yield increases depends on the specific angle chosen. The largest difference in yield (4.8x) is found at $\theta = 75$ °. Interestingly, at high angles of incidence, above 85°, Fig. 4 shows only a slight difference in the yield for H_2O–assisted milling compared with FIB sputtering. For example, at $\theta = 86$° the yield is only 1.5x that for FIB sputtering. We speculate that the effects of H_2O on yield are reduced at extremely high angles, because the adsorbed species are preferentially removed by the ion beam. Direct knock-on collisions with adsorbed species would reduce the surface concentration of reactive gas during a given scan making the interaction and yield similar to that for FIB sputtering. A reduced role of H_2O at very high angles may, in part, explain the smaller angle for which the maximum material removal rate is observed. We recognize that surface morphology may also affect the yield at high θ. As first observed by Russell et. al.,[14] the introduction of H_2O leads to a dramatically smooth surface compared with that produced by FIB sputtering at high incidence angles. The difference in step density may thereby lead to a vastly different ion reflection coefficient, and this could contribute to a decreased yield at high angles.

Measurements of $Y(0°)$ for H_2O-assisted milling are consistent with Russell et. al.[14], even though our value, 6.4 atoms/ion, is considerably less than that reported previously. This discrepancy is explained in the next section as being due to different ion beam pixel dwell times. The 130 μs dwell time used for experiments highlighted in Fig. 3.4 was chosen

more for convenience than for optimizing yield. Strategies for gas-assisted milling at maximum rates are developed by fixing the gas pressure at a reasonably high value and varying the pixel dwell time over a large range.[31,32]

Effect of Pixel Dwell Time on Yield for H_2O–assisted FIB Milling

Enhancement of etching by reactive gases has been modeled previously as a function of ion/neutral flux ratio and reactive gas coverage.[33,34] For the case of a focused beam rastered over a surface, continuous gas adsorption will occur in a given pixel, while material removal occurs only when the beam is on that pixel. Reactive gas is also removed during sputtering, such that the average surface coverage by reactive species depends on the pixel dwell time; we may expect that the observed etch yield will depend on the pixel dwell time. This has indeed been observed by Stark et. al.[21] in focused ion beam etching of PMMA using H_2O as a reactive gas.

In Fig. 3.5 we show that yield increases with decreasing pixel dwell time for H_2O enhanced etching, while there is no change in yield in the absence of H_2O. The origin of this effect is shown quite simply by considering the adsorption and ion-induced desorption kinetics of reactive gas. During the beam-off period gas adsorbs to the surface and the fractional coverage, C, can be described by a simple Langmuir adsorption process:

$$dC/dt = sf_n (1-C) \qquad (1a)$$

where s is a sticking coefficient and f_n is the flux of neutral species to the surface. Adsorption continues up to a monolayer and saturates when adsorption sites are exhausted.

During the beam-on period reactive species adsorb, as above, and are removed by sputtering. Some fraction of the removed species contain a substrate atom, and thus result in etching. The fractional coverage of gas then is described as

$$dC/dt = sf_n (1 - C) - bf_i C \quad (1b)$$

where b is the ion yield of reactive gas species (including carbon containing products), and f_i is the ion flux. The total etch yield, Y_{total}, is then the summation of the chemically-enhanced etching yield and the physical sputtering yield:

$$Y_{total} = jbC + Y_s(1 - C) \quad (1c)$$

where j is the fraction of reactive product species that contain a carbon atom, and Y_s is the sputter yield in the absence of chemical enhancement.[34] For simplicity we write the reactive etch yield as proportional to the surface coverage, assume all reactive products contain carbon (j=1), and assume simple Langmuir adsorption kinetics. In reality the situation may be more complicated due to surface alteration by ion mixing, and other ion bombardment induced effects that change the surface composition over the range of ion penetration. The chemically enhanced yield, b, strictly refers to removal of adsorbed gas, not to removal of substrate atoms, so the actual yield of substrate atoms will be less than b, and depend on the stoichiometry of the etch products. The sticking coefficient of reactive gas may also be different during the beam-on and beam-off periods due to the effects of ion bombardment in

producing defects and dangling bond sites, which are known to increase surface reactivity.[34] The yield parameters are also dependent on ion beam incidence angle. Despite these complications, this simple model has been shown effective at describing ion-enhanced etching of Si and SiO_2 in steady state plasma conditions.[33-35] We will show here that it also accounts for the yield dependence on pixel dwell time shown in Fig. 3.5 and in Stark's work.[21]

The beam is rastered over a 62 x 62 pixel array within the 12 x 12 μm box[36], and the 0.6 μm FWHM beam overlaps about 5 pixels at a time. Considering this pixel overlap we estimate the relative on/off periods of the beam as 1/1536. Using Equation 1a we calculate the surface coverage achieved during the beam-off period, then use Equation 1b to calculate the coverage during the beam-on period. During the beam-on period the coverage is

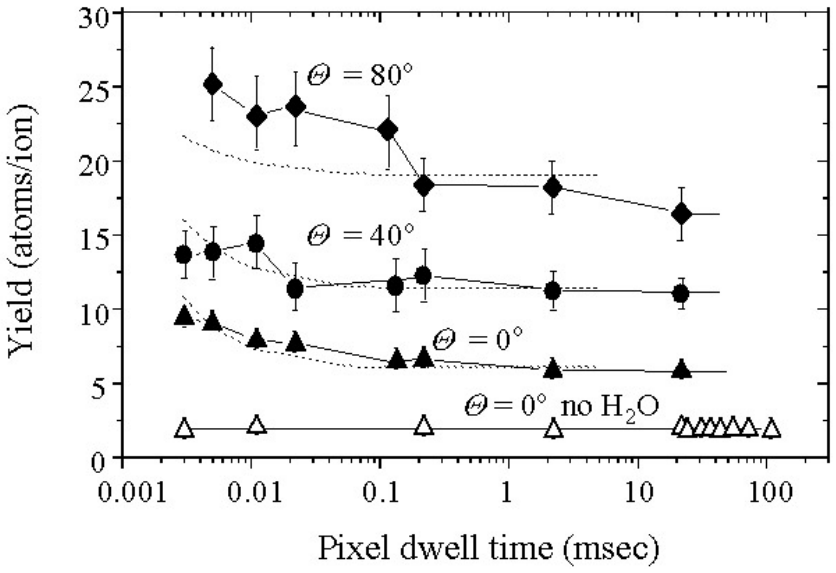

Figure 3.5. Plot of yield (C atoms/ ion) versus pixel dwell time for H_2O-assisted FIB milling of diamond (filled symbols) and FIB sputtering (Δ). Milling experiments at three different angles of incidence show the influence of pixel dwell time when using a fixed H_2O pressure. Dotted lines shown are simulated yields.

reduced by sputtering, and the etch yield in Equation 1c, is obtained from the average coverage during the beam-on period. Using the ion and neutral fluxes of the experiment, assuming unit sticking probability, and using the measured sputter yield in absence of H_2O enhancement, Y_s, we calculate the surface coverage and total etch yield, using the H_2O-enhanced yield, b, as the single adjustable parameter. Shown also in Fig. 3.5 are the calculated yields as a function of pixel dwell time, using H_2O-enhanced yields of 40, 40 and 25 for incidence angles of 0, 40, 80^o, respectively. The major effect noted in these simulations is that depletion of the reactive species coverage by sputtering during the beam-on period results in low average surface coverage for long pixel dwell times. Sufficient gas flux is available to saturate the surface during the beam-off period, but in these conditions of relatively low neutral/ion flux ratio, the surface is depleted of reactive species by sputtering for all but the highest angle of incidence (where the ion current density is low), and the average coverage is low. Short dwell times result in less depletion, and thus larger average coverage and higher etch yield. At long dwell times the yield is characterized by the steady state water coverage, similar to what would be observed in a reactive ion etching process at similar ion/neutral flux ratio.

The magnitude of the chemically enhanced yields used to fit these data seem reasonable. The interpretation being that at saturated water coverage, 40 carbon atoms should be removed per ion at normal incidence. The observed yields are substantially lower, because the average H_2O concentration during the beam-on period is typically well below saturation. This is realistic, but we should note a number of limitations of both the model and the experiment. First, we cannot independently measure surface coverage, so we must imply that all H_2O is removed from the surface by reaction with C (j=1). We know

that this is unlikely, but do not have a method for measuring the coverage or the composition of sputtered species. Second, we assume that H_2O adsorbtion saturates at a monolayer. There is evidence that multilayers of H_2O can adsorb, and the effects of ion mixing can result in substantially larger concentrations of reactive species incorporated into sub-surface layers as well.[18,37,38] These ion-mixing effects are known to be greater at near-normal incidence, hence the larger effect at $0^o$and 40^o as compared to 80^o. Third, we assume that the yield of carbon sputtered from areas not covered by water is the same as the yield observed in the total absence of water. The alteration of the surface layer by H_2O incorporation and ion damage may significantly change the surface binding energy of C, and hence the yield, even if no adsorbed water is present. Despite these complications, this simple model describes in a straightforward way the dependence of etch yield on pixel dwell time. The obvious strategy to achieve the highest etch yield is to use as high neutral/ion flux ratio as possible, and the shortest possible dwell time to maintain high surface concentration of reactive species.

The yields for H_2O-assisted FIB milling at 0^o shown in Fig. 3.5 are less than the value determined by Russell et. al.[14] because of the different pixel dwell times used in the two sets of experiments. Russell reports a pixel dwell time of 0.5 μs for their experiments and determines a yield of 14.4 atoms/ion. Extrapolation of the $\theta = 0^o$ data set shown in Fig. 5 to dwell times ~ 0.5 μs predicts a yield > 10 atoms/ion.

As a final note, previous work has shown that an increased material removal rate can be induced at high pixel dwell times when the depth removed per pixel is similar in dimension to the beam width.[39] This effect, which can occur with or without gas assist, is due to formation of a facet with a locally higher angle of incidence and higher yield (as in

Fig. 3.4). However, we are confident that this does not occur to a large degree in our experiments, since the ion beam FWHM is considerably larger than the depth removed per pixel even for the largest pixel dwell times.

Surface Morphology and Effects of H_2O

Different surface morphologies develop during ion bombardment depending on the angle of incidence and the presence / absence of H_2O. As shown in Figs. 3.2 and 3.6, three distinct morphologies are observed: smooth surfaces, ripples and a step/terrace topography. The dotted lines shown in the two plots of Fig. 3.6 bound ranges of angles where surfaces show one of the three distinct shapes. This figure also displays the roughness measured by a Digital Instruments Dimension 5000 atomic force microscope using a ~5 nm radius tip. The roughnesses are obtained by scanning 5 x 5 μm areas in the center of ion milled features.

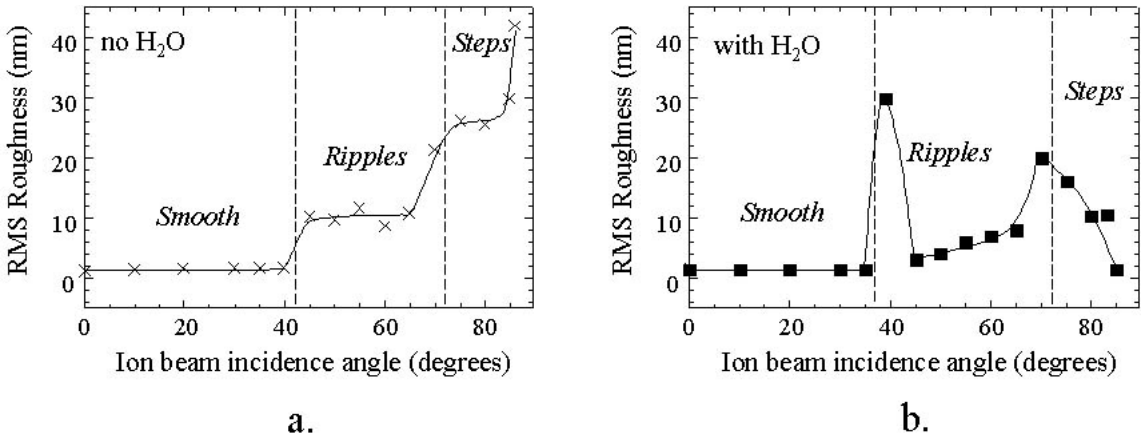

Figure 3.6. Plots of root mean squared surface roughness (R_{rms}) versus angle of incidence for (a.) FIB sputtering and (b.) H_2O-assisted FIB milling. Measurements of roughness and determination of morphology involved atomic force microscopy.

For θ less than 40°, FIB sputtering and H_2O-assisted milling generate smooth surfaces. The roughness of ion bombarded surfaces is small with $R_{rms} \sim 1.5$ nm for both processes. Comparison of the surface roughness in the bottom of ion bombarded features to that of the surrounding areas not exposed to the beam shows that the milled surfaces are smoother. These observations are consistent with a previous investigation of FIB sputtered diamond.[40]

At higher angles of incidence, ripples develop during FIB sputtering and H_2O-assisted FIB milling. The formation of ripples during oblique ion bombardment has been observed previously for a number of material systems[41-43], and models have been proposed to explain ripple frequency and amplitude as a result of ion scattering parameters and surface transport processes.[44,45] Ripples grow as a result of a surface instability induced by a subtle dependence of sputter yield on surface curvature.[44] Smoothening mechanisms can include thermal diffusion[44,46], viscous flow[47], ion-enhanced diffusion[48,49] and preferential sputtering without mass transport.[45] Thermal diffusion on diamond at 30°C is unlikely[50], but the fact that we observe surface smoothing at normal incidence (where ripples do not form) suggests that some ion enhanced transport process is involved. In these experiments an amorphous layer near the surface is formed by ion bombardment (see the following section), so viscous flow as well as ion enhanced surface diffusion is possible. However we cannot distinguish between these two ion-induced processes. A more comprehensive examination of ripple formation and evolution with dose is presented in another paper.[51]

Ripples developed during FIB sputtering[40] and H_2O-assisted FIB milling have a wavevector aligned with the projection of the ion beam vector. Fig. 3.7 shows atomic force microscope images of rippled surfaces formed at $\theta = 55°$ demonstrating this single habit that

continues to high θ. A second mode of ripples having a perpendicular orientation is found in other experiments and is predicted by Bradley and Harper,[44] but we find no evidence for a transition to ripples having this orientation. We show in a separate study[51] that for 20 keV Ga^+ the transition to perpendicularly oriented ripples is predicted to occur near 73^o. Essentially the deposited energy distribution resulting from Ga ion bombardment extends the transition in ripple habit to relatively high angles, compared with that for low energy ion bombardment. [52] Above 70^o we observe the transition from parallel ripples to a distinct step/terrace structure. This sawtooth-like morphology is evidence that shadowing becomes important at $\theta > 70^o$. Shadowing between isolated surface morphological features occurs, because a critical feature height/length ratio is exceeded thereby preventing ion beam exposure to parts of the surface.[53] The result is planarization of the peaks on the surface and formation of distinct terraces and step risers. It is apparent that shadowing and the formation of a step/terrace morphology thereby precludes the onset of ripples having a perpendicular-orientation in diamond. We expect this to be a general phenomenon in other materials FIB sputtered at high energy.

Although FIB sputtering and H_2O-assisted FIB milling both generate ripples of a single orientation, there are noticeable differences in morphology formed by the two processes. First, the lowest angle at which ripples develop is different for FIB sputtering compared with reactive milling. For FIB sputtering (no gas assist) we find ripples beginning at $\theta = 45^o$. This is consistent with previous work by Datta et. al.[54] at 10 and 50 keV. With the addition of H_2O, ripples clearly form at a smaller angle $\theta = 40^o$. Although the ripple onset angle has previously been observed to change with ion beam energy,[54] we believe that this is the first report showing a change in angle due to the presence of a reactive gas. Other differences in ripple morphology are apparent by atomic force microscopy (AFM). Comparisons of surfaces show that H_2O-assisted etching on average leads to a reduced ripple wavelength and amplitude. The two images shown in Fig. 3.7 compare FIB sputtered and reactively milled surfaces for a single angle of incidence, 55^o. We find in a separate study of evolving ripple shape with increasing dose[51] that a near-

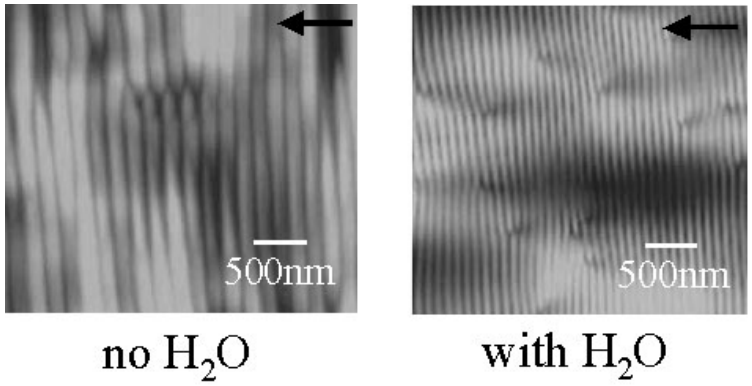

Figure 3.7. AFM images of diamond surface FIB sputtered (left) and FIB milled in the present of H_2O (right). Experiments involved a single ion beam incidence angle, $\theta = 55^o$, and a fixed dose of $1x10^{19}$ ions/cm^2. Arrows indicate the projection of the ion beam vector. Reduced ripple wavelength is shown when using H_2O.

constant wavelength characterizes the surface morphology at high ion doses. This evolution to a steady-state morphology is observed in other materials and appears to be a somewhat general behavior.[40,43] Fig. 3.8 shows the saturation wavelength, λ^*, as a function of incidence angle. For all angles the saturation wavelengths for FIB sputtering are larger than that developed during H_2O-assisted FIB milling.

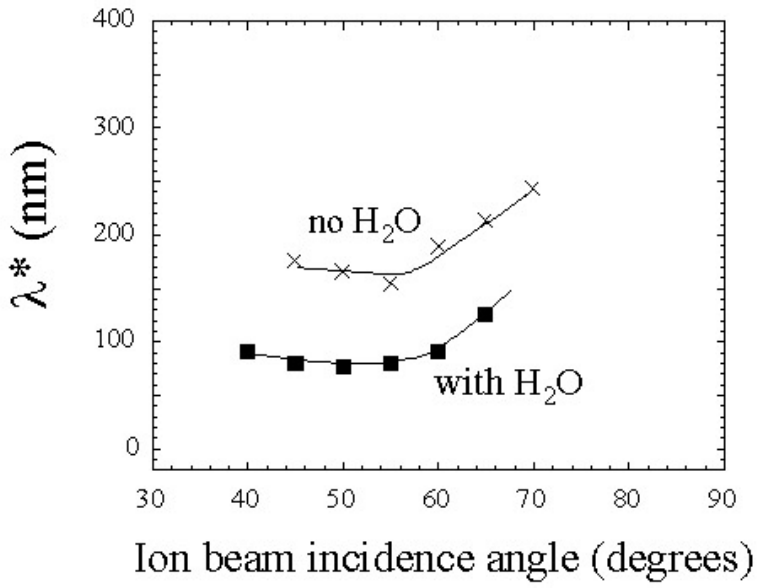

Figure 3.8. Plot of saturation ripple wavelength (λ^*) versus ion beam incidence angle. This contrasts λ^* for FIB sputtering and H_2O-assisted FIB milling.

We argue that the differences in ripple wavelength produced by the two processes are due to reactive gas adsorption and its effect on increasing yield.[51] The roughening prefactor described by Bradley and Harper[44] is proportional to yield, and the λ^* derived (for the case of thermal diffusion) is inversely related to the square root of $Y(\theta)$. Assuming that a similar relationship exists for the case of ripple development in carbon, the higher gas-assisted milling yields shown in Fig. 3.4 for θ between 45 and 65^o should lead to a decrease in λ^* by as much as a factor of 2. This is precisely the result shown in Fig. 3.8 when comparing results from FIB sputtering and H_2O-assisted milling. For each θ studied, the saturation wavelength is decreased by approximately a factor of 2 when H_2O is present.

A curious surface morphology develops at $\theta = 40^o$ when using H_2O (see Fig. 3.9). At this angle H_2O-assisted etching leads to a dramatically rougher surface than for FIB sputtering with no gas assist (R_{rms} = 30 nm compared with R_{rms} = 1 nm). Ripples develop during H_2O-assisted ion milling at 40^o with wavelength similar to those observed at higher angles. Additionally, we observe very large amplitude, poorly aligned ridges with much longer wavelength than the well oriented ripple structures shown. The large amplitude ridges dominate the surface roughness spectrum at 40^o, leading to the anomalous rms roughness value shown in Fig. 3.6.b. Ridges are still evident in the morphology observed at higher angles, but not nearly to the extent as at 40^o. We do not know the nature of the dynamic processes driving this development. We observe an interesting effect of pixel dwell time on surface morphology evolution at 40^o. The very large amplitude, low frequency surface features are apparent at short dwell times but disappear at long dwell times. As noted earlier, for long dwell times the average surface coverage by water is low, and most etching takes place at relatively 'dry' sputtering conditions. The development of

this gross morphology is evidently an effect of water adsorption during sputtering, and is most prominent at conditions of high surface coverage. The reason why the effect is confined primarily to angles near 40^{o} is also unknown.

At high angles of incidence ($\theta > 70^{o}$) a step/terrace morphology is observed. This is highlighted in Fig. 3.10 for surfaces FIB sputtered at 75 and 86^{o}. This different morphology more closely resembles a sawtooth waveform rather than a sinusoid ripple formed at lower angles. Transmission electron microscopy (TEM) images in Figs. 3.11 and 3.12 further contrast the two types of morphology formed at different angles. A step/terrace morphology is an accurate description of the surface formed at high angles compared with previous

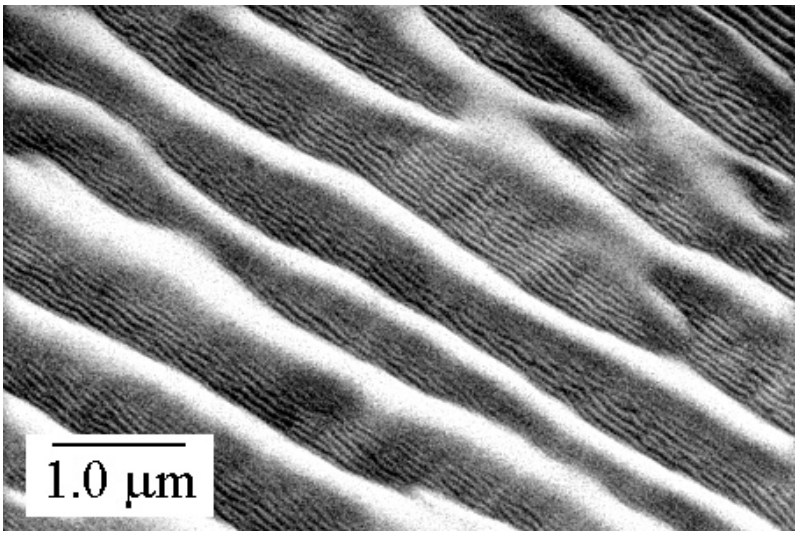

Figure 3.9. Scanning electron micrograph of surface FIB milled in the presence of H_2O at $\theta = 40^{o}$. High frequency ripples ($\lambda \sim 90$ nm) are seen in addition to large amplitude, long wavelength ($\lambda \sim 1000$ nm) ridges. The long wavelength features are only seen when using H_2O assist and are most prominent at $\theta = 40^{o}$.

discussions of this being a 'facetted' shape.[53] While the TEM in Figure 3.12 shows well-defined terraces, step risers have curved profiles and a range of angles with respect to the ion beam vector.

A step/terrace morphology is explained by shadowing between neighboring surface morphological features.[53] Shadowing can occur because of texture initially present on the surface or possibly ripples that develop for some short period of time.[53] We have found that a step/terrace morphology can evolve from an initial ripple morphology as the amplitude of the ripples grows at angles around 70^{o}.[55] Essentially because the beam is approaching at such a high angle it will not access all of the surface if features of a certain height / length ratio are present. The ion flux preferentially sputters the peaks of the protrusions and local planarization occurs. The surface then evolves to have a step/terrace morphology.[53] Carter has shown that a critical height to wavelength ratio exists where shadowing sets in at a particular incidence angle.[53] This amplitude to wavelength ratio is given by:

$$A/\lambda \leq 1/2\pi \tan(\pi/2-\theta)$$

At a fixed angle terraces will be longer if the amplitude is increased. After high doses, terraces of greater length win out at the expense of shorter length terraces that exist for only a brief time.

We also observe that the average terrace length changes with θ for both FIB sputtering and H_2O-assisted FIB milling. Terraces are longer as the angle of incidence is increased. This is indicated in Fig. 3.10; FIB sputtering at 75° results in terraces that are 0.2-0.5 μm long, while for θ ~86° FIB sputtered surfaces have terraces that are 2-20 μm in length. AFM also shows that the terraces are parallel to the ion beam at high ion doses. In this case ions incident on the terraces at very grazing angles will likely be reflected and impact the next step riser. In the extreme case, all ions eventually impact on step risers. The step riser will move laterally over the surface with a rate determined by the sputter yield at the local angle of incidence on the step riser. In this scenario, the terrace length will be determined by the height of the step riser and the critical angle for sputtering.

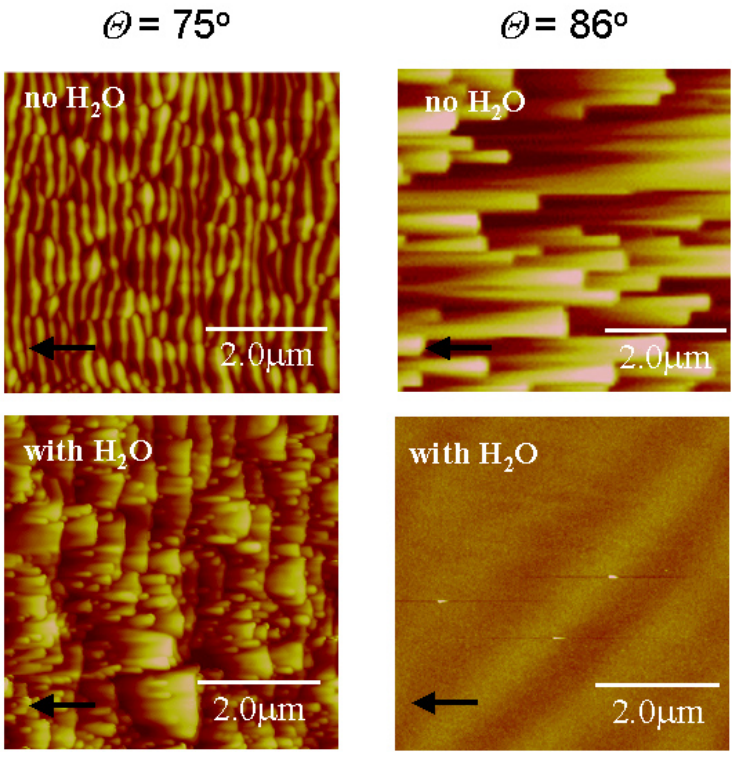

Figure 3.10. AFM images of diamond FIB sputtered and milled at two high angles of incidence. All images are taken on a 100 nm vertical scale.

As indicated in Figs. 3.6 and 3.10, introduction of H_2O during ion bombardment dramatically reduces the amplitude of the step risers and the overall surface roughness.[14] For increasing angle greater than 70^o, the surface roughness decreases for H_2O-assisted milling, while FIB sputtering leads to increasingly rough surfaces up to 86^o. At 85^o the reactively milled surface has a R_{rms}=1.0 nm, a 30-fold reduction in roughness compared with that for sputtering.

We suggest that the $Y(\theta)$ for a given process is responsible for the differences shown in Fig. 3.10 at 86^o. Specifically, the difference in yield at localized microscale sites on the surface will give rise to a different steady-state (high dose) morphology. Based on the images shown in Fig. 10, a difference in sputter yield must exist for the step riser versus the terrace for the case of FIB sputtering. In this way, a step riser can be slow to propagate across the surface and the surface develops rough. For the case of H_2O-assisted milling we expect more similar sputter yields at different sites on the surface. In order to assess the real difference in sputter yield on a riser versus a terrace, one must determine yield at each particular angle when using a flat target surface. Real time dynamic observations of the surface morphology would aid in the understanding of H_2O assisted smoothing of the ion milled diamond surface. A more complete study should probe lateral step velocities as a function of step height.

Microstructure and Effects of H_2O

Cross section transmission electron microscopy shows that high-energy ion bombardment amorphizes the near-surface region of diamond substrates. A damaged layer is evident in Figs. 3.11 and 3.12 for FIB sputtering at 55 and 80°, respectively. TEM also indicates a variation in amorphous thickness at different sites on rough surfaces. In general, a larger amorphous thickness develops at sites having a small local angle of incidence with respect to the ion beam. A clear example of this is seen in Fig. 3.12 where the step riser has an amorphous thickness of approximately 30 nm and the terrace (at near grazing incidence) is damaged to a depth of 12 nm. TEM also shows no evidence that surface morphological features are aligned to low Miller index orientations of the crystalline substrate. This includes the terraces formed at $\theta > 70^{o}$ which tend to align close to the direction of the ion beam vector.

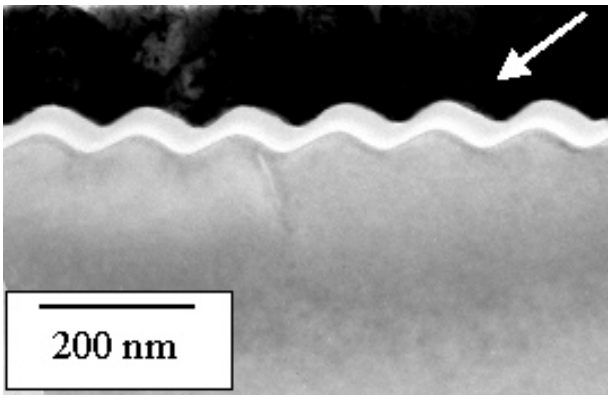

Figure 3.11. Transmission electron micrograph of rippled surface. This sample was FIB sputtered at $\theta = 55^{o}$ with the beam direction indicated by an arrow. The amorphized region formed as a result of ion beam damage appears as a 'bright' feature.

The effects of H_2O on microstructure are also revealed by TEM. In general, a 20 % reduction in the amorphous thickness is found when using gas-assisted FIB milling. Fig. 3.13 shows an example of this for bombardment at $\theta = 0^o$. We choose this angle for analysis, because a smooth surface and uniform amorphous carbon layer thickness are developed. Control experiments show that H_2O does not spontaneously etch a FIB-damaged carbon surface. No change in feature depth was observed after exposing a pre-milled surface to a flux of H_2O for many minutes (with the ion beam off). Therefore, we can expect that the reduction in layer thickness is an effect of reactive sputtering. The difference in amorphized thickness is consistent with an enhanced material removal rate for H_2O-assisted processes compared with FIB sputtering.

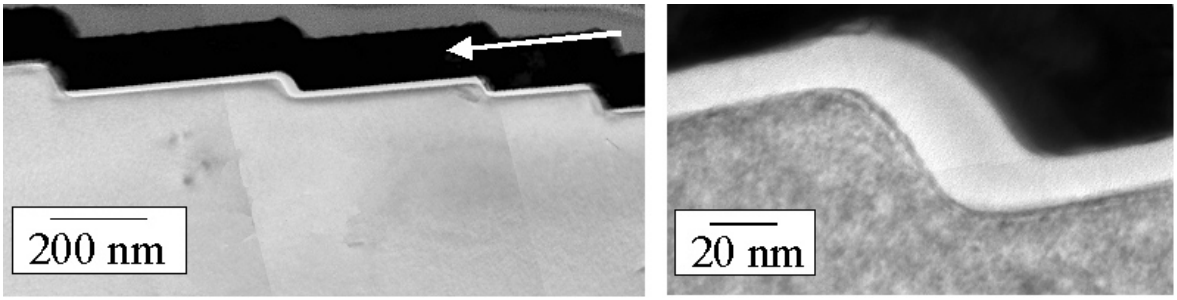

Figure 3.12. Transmission electron micrographs showing FIB sputtered surface in cross section. Sputtering involved $\theta = 80^o$ and a dose of 10^{17} ions/cm^2. Step/terrace morphology is evident along with a damaged layer that varies in thickness from step riser to terrace. The beam direction is indicated by an arrow.

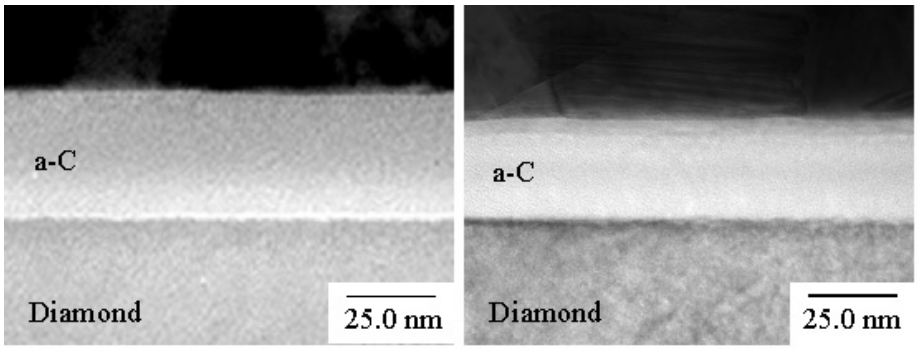

Figure 3.13. Transmission electron micrographs showing the damage layers resulting from FIB sputtering (left) and H_2O-assisted FIB milling. Sample was bombarded with Ga^+ at $\theta = 0^o$ to 10^{18} ions/cm^2. 'a-C' indicates the damaged region.

3.4 Summary

FIB sputtering and H_2O-assisted FIB milling of initially single crystal diamond surfaces result in very different yields (defined as the number of C atoms removed per incident gallium ion). Consistent with Russell et. al.[14] we find an increase in material removal rate when using H_2O - assisted processes. This is now demonstrated across a broad range of angles with the enhancement in yield depending on the specific angle chosen. We find large yield enhancements at $\theta \leq 75^o$, yet water has a small effect on yield at very high angles of incidence ($\geq 85^o$). Possible explanations for this are discussed. The enhancement in yield due to H_2O also depends on ion /neutral flux. A strategy for maximizing the yield involves selecting a small pixel dwell time.

The surface morphology developed during ion bombardment changes with ion beam incidence angle and the addition of H_2O. We find a single mode of ripples to high angles of incidence for both FIB sputtering and H_2O assisted FIB milling. This single ripple habit is

due to the deeply penetrating nature of high-energy ions and is predicted to occur in other material systems that exhibit a ripple morphology when using similar beam energies and ion species. H_2O affects this morphology in two ways. First, it lowers the angle of ripple onset. Ripples form at 40^o when using H_2O-assisted milling techniques, whereas FIB sputtering generates ripples beginning at 45^o. Furthermore, a reduced saturation ripple wavelength results from H_2O exposure. A reduced wavelength is explained by an increased $Y(\theta)$ when using H_2O-assisted milling. Dramatic differences in step/terrace morphology are found for angles > 70^o. Surfaces are smoother when using H_2O for all angles $\theta > 70^o$.

Strategies for diamond microfabrication can be developed from the observations made in this work and previous studies. Microfabrication time can clearly be reduced by choosing the angle at which a maximum yield occurs and adding H_2O vapor. The effects of H_2O on yield are further increased when selecting small pixel dwell times. Nevertheless, H_2O – assisted milling techniques offer only a limited improvement in surface finish. If a smooth surface is desired one can work in the range of angles ($\theta < 40^o$ or $\theta \geq 85^o$) where no ripples or steps develop. High-angle, H_2O-assisted FIB milling is useful for making smooth surface, planar cuts. On the other hand, fabrication of curved surfaces to intermediate angles requires careful thought. A smooth-surface, hemispherical or parabolic microindenter will be difficult to fabricate from an initially flat-face tool blank if the ion beam vector is kept parallel to the axis of the indenter. For fabricating curved shapes, angles >40^o lead to undesired roughness that cannot be overcome solely by the addition of H_2O. Note, fabrication of nanoscale indenters, such as those having diameters less than a single ripple wavelength, may show different morphologies than those presented here.

Alternatively, recipes have now been developed that reproducibly create patterned surfaces of different shape. The formation of a regular array of ripples having a well-defined wavelength and amplitude and a step / terrace morphology having a distribution of terrace lengths could find use as a surface templating technique for subsequent thin film growth.

3.5 References

1. J. Orloff, Rev. Sci. Instrum. 64(#5), (1993) 1105-1130.

2. M.J. Vasile, C. Biddick, and S. Schwalm, J. Vac. Sci. Technol. B12 (1994) 2388.

3. Y.N. Picard, D.P. Adams, and M.J. Vasile, J. Precision Engineering, 27(2003) 59-69.

4. J.P. Sullivan, T.A. Friedmann and K. Hjort, MRS BULLETIN 26(#4) (2001) 309-311.

5. E. Kohn, P. Gluche, and M. Adamschik, Diamond Relat. Mater. 8 (1999) 934.

6. T. Shibata, Y. Kitamoto, K. Uhno, and E. Makino, J. Microelectromech. Syst. 9 (2000) 47.

7. J. Taniguchi, J. Yokoyama, M. Komuro, H. Hiroshima, and I. Miyamoto, Microelect. Eng. 52 (2000) 415-418.

8. K.F. Jarausch, PhD Dissertation: *Nanomechanics of Thin Films and Surfaces* (1999, North Carolina State University).

9. I. Miyamoto, S. Kiyohara, M. Ide, M. Itami and S. Honda, Int. J. Japan. Soc. Prec. Eng., 29 (1995) 295. A. Olbrich, B. Ebersberger, C. Boit, P. Niedermann, W. Hanni, J. Vancea, and H. Hoffmann, J. Vac. Sci. Technol. A 17 (1999) 1570.

10. D. P. Adams, M.J. Vasile, and A.S.M. Krishnan, J. Precision Engineering, 24, (2000) 347-356.

11. C.A. Brookers, in *The Properties of Natural and Synthetic Diamond*, edited by J.E. Field (Academic, New York, 1992), 515.

12. J.E. Field, in *Properties and Growth of Diamond*, edited by Gordon Davies (INSPEC, the Institution of Electrical Engineers, London, 1994), 52-53.

13. J. Taniguchi, N. Ohno, S. Takeda, I. Miyamoto, and M. Komuro, J. Vac. Sci. Technol. B16 (1998) 2506-2510.

14. P.E. Russell, T.J. Stark, D.P. Griffis, J.R. Phillips, and K.F. Jarausch, J. Vac. Sci. Technol. B16(#4) (1998) 2494-2498.

15. A. Stanishevsky, Thin Solid Films 398-399 (2001) 560-565.

16. measured previously for graphite substrates, see E. Vietzke, A. Refke, V. Philipps, and M. Hennes, J. Nucl. Mat. 241-243 (1997) 810-815.

17. L.R. Harriott, Jpn. J. Appl. Phys. Part 1, 33 (1995) 7094.

18. H.F. Winters, J.W. Coburn, Surf. Sci. Rep. 14 (1992) 161-269.

19. N.N. Efremow, M.W. Geis, D.C. Flanders, G.A. Lincoln, and N.P. Economou, J. Vac. Sci. Technol. B3 (1985) 416-418.

20. P.E. Russell, D.P. Griffis, G.M. Shedd, T.J. Stark and J. Vitarelli, U.S. Patent # 6,140,655. Method for Water Vapor Enhanced Charged-Particle-Beam Machining, issued Oct. 31, 2000.

21. T.J. Stark, G.M. Shedd, J. Vitarelli, D.P. Griffis, and P.E. Russell, J. Vac. Sci. Technol. B 13 (1995) 2565-2569.

22. A. Datta, Y-Ron Wu and Y.L. Wang, Appl. Phys. Lett. 75 (1999) 2677-2679.

23. P. Sigmund, Phys. Rev. 184 (1969) 383.

24. M.J. Vasile, J. Xie and R. Nassar, J. Vac. Sci. Technol. B 17(#6) (1999) 3085-3090. M.J. Vasile, R. Nassar, J. Xie and H. Guo, Micron 30 (1999) 235-244.

25. L. Harriott , Proc SPIE, 773 (1987) 190.

26. M.J. Vasile, C. Biddick and S. Schwalm, Proc. of the ASME, DSC, 46 (1993) 81.

27. Atomic force microscopy and interferometric microscopy measurements show an initial surface roughness, R_{rms}, of 2.0-3.0 nm.

28. This represents the total time to complete a single scan and return to the starting pixel.

29. *CRC Handbook of Chemistry and Physics*, 79th Edition, (CRC Press, 1998) p. 4-140.

30. TRIM calculations of Y(θ) model Ga ion impingement on diamond flat surface, assuming a lattice binding energy of 3 eV, a surface binding energy of 7.4 eV and a displacement energy of 28 eV.

31. I. Chyr and A.J. Steckl, J. Vac. Sci. Technol. B 19 (2001) 2547.

32. R.J. Young, J.R. Cleaver and H. Ahmed, J. Vac. Sci. Technol. B 11 (1993) 234.

33. R.A. Barker, T.M. Mayer and W.C. Pearson, J. Vac. Sci. Technol. B 1 (1983) 37. T. Mizutani, C. J. Dale, W. K. Chu, T. M. Mayer, Nucl. Instr. Meth. B 7/8 (1985) 825.

34. J.P. Chang, J.C. Arnold, G.C.H. Zau, H-Shik Shin, and H.H. Sawin, J. Vac. Sci. Technol. A 15 (1997) 1853.

35. T. M. Mayer and R. A. Barker, J. Vac. Sci. Technol. 21, 757 (1982).

36. A scan size of 100 x 100 μm was selected prior to defining the 12 x 12 μm box. The larger area consists of a 512 x 512 array of pixels.

37. E. L. Barish, D. J. Vitkavage, and T. M. Mayer, J. Appl. Phys. 57, 1336 (1985).

38. J. Dieleman, F.H.M. Sanders, A.W. Kolfschoten, P.C. Zalm, A.E. de Vries and A. Haring, J. Vac. Sci. Technol. B 3 (1985) 1384.

39. Essentially this condition leads to the formation of a different facet angle under the beam that can have a higher yield. See D. Santamore, K. Edinger, J. Orloff and J. Melngailis, J. Vac. Sci. Technol. B, 15 (1997) 2346.

40. A.Datta, Y-Renn Wu, and Y.L. Wang, Phys. Rev. B 63 (2001) 125407.

41. T.M. Mayer, E. Chason and A.J. Howard, J. Appl. Phys. 76 (1994) 1633.

42. G. Carter and V. Vishnyakov, Phys. Rev. B 54 (1996) 17647.

43. J. Erlebacher, M.J. Aziz, E. Chason, M.B. Sinclair and J.A. Floro, Phys. Rev. Lett 82 (1999) 2330-2333.

44. R.M. Bradley and J.M.E. Harper, J. Vac. Sci. Technol. A 6 (1988) 2390-2395.

45. S. Park, B. Kahng, H.Jeong, and A.-L. Barabasi, Phys. Rev. Lett. 83 (1999) 3486. M.A. Makeev and A.-L. Barabasi, Appl. Phys. Lett. 71 (1997) 2800.

46. C. Herring, in *Physics of Powder Metallurgy* (McGraw-Hill, New York 1951), p.143.

47. E. Chason, T.M. Mayer, B.K. Kellerman, D.T. McIlroy, and A.J. Howard, Phys. Rev. Lett. 72 (1994) 3040.

48. S.M. Rossnagel, R.S. Robinson, and H.R. Kaufman, Surface Sci. 123 (1982) 89.

49. S.W. MacLaren, J.E. Baker, N.L. Finnegan, and C.M. Loxton, J. Vac. Sci. Technol. A 10 (1992) 468.

50. E.A. Eklund, R. Bruinsma, J. Rudnick and R.S. Williams, Phys. Rev. Lett. 67 (1991) 1759.

51. T.M. Mayer, D.P. Adams, and M.J. Vasile, to be published (2003).

52. I. Koponen, M. Hautala, O.P. Sievänen, Phys. Rev. Lett. 78 (1997) 2612. S. Habenicht, K.P. Lieb, W. Bolse, U. Geyer, F. Roccaforte, and C. Ronning, Nucl. Inst. and Methods, 161-163 (2000) 958-962.

53. G. Carter, J. Appl. Phys. 85 (1999) 455-459.

54. Previous FIB sputtering (without gas assist) by Datta et. al. (reference 40) shows the onset of ripples in diamond at $\theta = 40^{o}$ for E = 50 keV and at $\theta = 50^{o}$ for E = 10 keV.

55. D.P. Adams, T.M. Mayer and M.J. Vasile, to be published (2003).

Acknowledgements

The authors appreciate the efforts of J. Michael (SNL), K. Archuleta (SNL), M. Barry Ritchey (SNL), Y. Picard (University of Michigan) and S. Moncrief at Louisiana Tech University (Ruston, LA). This work is supported by the United States Department of Energy under Contract No. DE-AC04-94AL85000. Sandia is a multiprogram laboratory operated by Sandia Corporation, a Lockheed Martin Company, for the United States Department of Energy.

Distribution:

1 MS0188 LDRD Office,
3 MS0959 D.P. Adams
1 MS0959 R.L. Poole
1 MS0959 M.J. Vasile
2 MS0899 Technical Library, 9616
1 MS9018 Central Technical Files, 8945-1